RESEARCH ARTICLE

Temporal Genomic Analysis of Homogeneous Tumor Models Reveals Key Regulators of Immune Evasion in Melanoma

Sapir Cohen Shvefel[1], Joy A. Pai[2], Yingying Cao[3], Lipika R. Pal[3], Osnat Bartok[1], Ronen Levy[1], Marie J. Zemanek[1], Chen Weller[1], Ella Herzog[4], Winnie Yao[2], Kamir J. Hiam-Galvez[2], Kuoyuan Cheng[3,5], Yajie Yin[2], Peter P. Du[2], Colin J. Raposo[2], Nofar Gumpert[1], Michele Welti[6], Julia M. Martínez Gómez[6], Federica Sella[6], Elizabeta Yakubovich[1], Irit Orr[7], Shifra Ben-Dor[7], Roni Oren[8], Liat Fellus-Alyagor[8], Ofra Golani[9], Ori Jacob Brenner[8], Tomer M. Salame[9], Mirie Zerbib[8], Inna Goliand[9], Dean Ranmar[9], Ilya Savchenko[8], Nadav Ketrarou[8], Alejandro A. Schäffer[3], Rony Dahan[4], Mitchell P. Levesque[6], Eytan Ruppin[3], Ansuman T. Satpathy[2,10,11], and Yardena Samuels[1]

ABSTRACT Low intratumor heterogeneity correlates with increased patient survival and immunotherapy response. However, even highly homogeneous tumors are variably aggressive, and the immunologic factors impacting aggressiveness remain understudied. In this study, we analyzed the mechanisms underlying immune escape in murine tumors with low intratumor heterogeneity. We used immunophenotyping and single-cell RNA sequencing to compare the temporal growth of *in vivo* transplanted, genetically similar, rejected and nonrejected single-cell clones. Nonrejected clones showed high infiltration of tumor-associated macrophages, lower T cell infiltration, and increased T cell exhaustion when compared with rejected clones. Comparative analysis of rejection-associated gene expression programs, combined with *in vivo* CRISPR knockout screens of candidate regulators, identified macrophage migration inhibitory factor (*Mif*) as a major contributor to preventing immune rejection. *Mif* knockout resulted in smaller tumors and reduced tumor-associated macrophage infiltration. These results were validated in patients with melanoma. Overall, our homogeneous tumor system can uncover factors regulating growth variability and identifies *Mif* as critical in aggressive melanoma.

SIGNIFICANCE: In this study, we find that *Mif* expression is associated with tumor growth and aggressiveness, specifically in tumors with low heterogeneity. These findings could facilitate the development of new strategies to treat patients with homogeneous, high *MIF*–expressing tumors that are unresponsive to immune checkpoint therapy.

INTRODUCTION

Tumors with low intratumor heterogeneity (ITH), as determined by the number of clones comprising the tumors and level of genomic clonal divergence, have been associated with improved survival and better responses to immunotherapy (1, 2). Although some factors correlate with this effect, why low ITH improves patient survival remains fundamentally unclear (3–8). Furthermore, patients bearing low-ITH tumors with aggressive disease show large variability in survival, indicating that other factors beyond ITH contribute to tumor aggressiveness and outcome (7, 9, 10). These observations motivated us to identify the factors contributing to immune escape in low-ITH tumors.

Tumor-associated macrophages (TAM) and cancer-associated fibroblasts correlate with an immunosuppressive tumor microenvironment (TME) and enhanced tumor growth (11–16). Such cell populations mediate protumorigenic effects by infiltrating the TME and modulating T cell proliferation and cytotoxicity (14, 17, 18). Indeed, TAMs inhibit the cytotoxic T cell response and promote neoangiogenesis, protumorigenic cytokine secretion, and epithelial–mesenchymal transition (19–23). TAMs also fuel cancer progression by promoting tumor outgrowth, invasion, and therapy resistance (24). Finally, TAM infiltration is associated with poor prognosis and tumor progression across cancers, including melanoma, pancreatic cancer, breast cancer, myeloma, renal cancer, and bladder cancer (11, 25–31).

However, the mechanisms underlying these correlations remain unclear. Genes underlying resistance mechanisms may explain TME characteristics in aggressive tumors. Although CRISPR screens and omic analyses have sought to identify these genes, the results are inconsistent, perhaps because of confounding effects such as tumor heterogeneity and the inclusion of genes that encode secreted factors, and their effects may be masked. Therefore, homogeneous, highly regulated systems are needed to identify factors linked to aggressive growth phenotypes and cell population shifts in the TME.

We hypothesized that the mechanisms responsible for aggressive tumor behavior could be investigated in low-ITH patients by establishing a novel experimental system that enables us to tease apart which TME factors play a role in aggressive tumor growth in low-ITH settings. This system

[1]Department of Molecular Cell Biology, Weizmann Institute of Science, Rehovot, Israel. [2]Department of Pathology, Stanford University, Stanford, California. [3]Cancer Data Science Laboratory, Center for Cancer Research, National Cancer Institute, Bethesda, Maryland. [4]Department of Systems Immunology, Weizmann Institute of Science, Rehovot, Israel. [5]MSD R&D (China) Co., Ltd, Beijing, China. [6]Department of Dermatology, University Hospital Zurich, University of Zurich, Zurich, Switzerland. [7]Bioinformatics Unit, Department of Life Sciences Core Facilities, Weizmann Institute of Science, Rehovot, Israel. [8]Department of Veterinary Resources, Weizmann Institute of Science, Rehovot, Israel. [9]Department of Life Sciences Core Facilities, Weizmann Institute of Science, Rehovot, Israel. [10]Gladstone-UCSF Institute of Genomic Immunology, San Francisco, California. [11]Parker Institute for Cancer Immunotherapy, San Francisco, California.

S. Cohen Shvefel and J.A. Pai are co-first authors of this article.

Corresponding Authors: Yardena Samuels, Weizmann Institute of Science, 234 Herzl Street, Rehovot 76100, Israel. E-mail: yardena.samuels@weizmann.ac.il; Ansuman T. Satpathy, Stanford University, 240 Pasteur Drive, Stanford, CA 94304. E-mail: satpathy@stanford.edu; and Eytan Ruppin, National Cancer Institute, Bethesda, MD 20892. E-mail: eytan.ruppin@nih.gov

Cancer Discov 2025;15:553–77

doi: 10.1158/2159-8290.CD-23-1422

builds on an *in vivo* mouse model [Wolf and colleagues (5)] to assess ITH effects independent of tumor mutational burden (TMB). Using this model, we compared the transcriptomic state of tumor and immune cells in rejected tumors with that in nonrejected tumors upon transplantation, thus identifying specific factors in homogeneous tumors that explain the large variability in the survival time of patients bearing low-ITH tumors. In-depth cellular analyses were performed across several time points during tumor evolution, followed by functional validation. We found that changes in *Mif* levels affected the TME and dictated tumor growth in mice, validating this association in patient data. Although *Mif* upregulation is associated with poor prognosis (32–36), its contribution to tumor aggressiveness and outcomes remains unclear (37, 38). Our experimental system revealed how MIF shapes the suppressive TME in homogeneous, low-ITH tumors *in vivo* and suggests potential approaches to improve immunotherapy for patients bearing such tumors.

RESULTS

Survival Time Is Variable in Patients with Low ITH

Previous studies indicate that patients with melanoma with low ITH exhibit improved survival compared with those with high ITH (1, 2). However, analysis of patients with high- versus low-ITH melanoma in The Cancer Genome Atlas (TCGA) revealed higher complexity. Although low-ITH patients had significantly higher survival than those with high ITH (Supplementary Fig. S1A, two-sided Mann–Whitney test, $P = 0.014$), the survival times of low-ITH patients were broadly distributed (IQR of 2,587 days for low-ITH patients vs. 1,452 days for high-ITH patients; Supplementary Fig. S1A). Indeed, 40% of the low-ITH patients exhibited a poor outcome, with lower survival time than the median survival of high-ITH patients [termed low-ITH, poor survival (LIPS) patients]. Notably, there was no significant difference between the survival times of these LIPS patients and the high-ITH patients (P value = 0.4; Supplementary Fig. S1B).

To follow up on this large variance in low-ITH patients, we compared immune characteristics in LIPS patients with high-ITH patients and assessed their T cell cytolytic scores (39) using bulk expression data. Cytolytic scores were significantly higher for LIPS patients than for those with high ITH (P value = 0.005; Supplementary Fig. S1C). Furthermore, low-ITH patients with high T cell cytolytic scores showed a significantly higher survival time than those with low cytolytic scores (Supplementary Fig. S1D).

A Mouse Model to Identify Factors Influencing Tumor Growth in Low-ITH Settings

The above analysis motivated us to identify factors facilitating tumor escape from immune surveillance. Therefore, we established an *in vivo* mouse model to identify novel factors contributing to enhanced low-ITH tumor growth. Wolf and colleagues (5) previously established a genetically heterogeneous cell line and derived low-ITH single-cell clones (SCC). The SCC-derived tumors showed enhanced $CD8^+$ T cell infiltration, fewer immunosuppressive $CD4^+$ regulatory T cells (Treg), and higher degranulation and cytotoxicity than high-ITH tumors. Based on this model, we exposed a mouse melanoma cell line (40) to UVB radiation, a key melanoma driver. This treatment increased ITH levels, creating a highly genetically heterogeneous population. Whole-exome sequencing (WES) of this UVB-irradiated sample revealed a TMB of 2,799 exonic mutations and variant allele frequency (VAF; defined as the frequency of a mutation within the population plotted against the probability density function) value of 0.189, which is lower than 0.25 and therefore highly heterogeneous (Supplementary Table S1; Supplementary Table Legends; ref. 41). From this heterogeneous parental line, we generated 40 homogeneous SCCs. WES analysis of SCC mutations verified that the clones harbored a narrow VAF distribution with the fraction of clonal single-nucleotide variants ranging from 0.835 to 0.949, indicating substantially lower ITH levels than the parental UVB-irradiated sample, and an average TMB of 1,765 (Supplementary Table S1; Supplementary Table Legends).

Phylogenetic analysis of data from the heterogeneous UVB cell line yielded a phylogenetic tree with eight terminal branches (TB; TB-1 to TB-8; Fig. 1A). We mapped the 40 SCCs to terminal branches of the tree based on sequence similarity. TBs were represented by clusters of 2 to 11 SCCs (Fig. 1A). We focused on TB-3, represented by six SCCs that shared clonal and subclonal mutations with an overall genetic similarity >80% (Supplementary Fig. S1E). Although five of these six SCCs showed reproducible growth when inoculated into immunocompetent C57BL/6 mice, two clones were rejected (SCC31 and SCC40) within 16 to 20 days of inoculation and three grew aggressively, escaped immune surveillance, and remained nonrejected (SCC32, SCC35, and SCC37; Fig. 1B). The VAF values of the five clones were similar, arguably because clonality does not explain the distinct phenotypes (Fig. 1C).

To test whether the growth impairment of SCC31 and SCC40 depended on the immune system, tumor volume was monitored after inoculation of these clones into NOD/SCID gamma (NSG) immunodeficient mice. All SCCs grew and formed tumors in immunodeficient mice (Fig. 1D), demonstrating that the immune system mediated tumor rejection. To confirm rejection, SCC31 cells were inoculated into mice, and tumor growth was monitored (Supplementary Fig. S1F–S1H). After tumor rejection, tissues surrounding the inoculation site were harvested and subjected to pathologic analysis (Supplementary Fig. S1I and S1J). Inflamed scar tissue at the tumor inoculation site showed a complete pathologic response, immune infiltration, and a wound healing bed at the site, confirming rejection. WES data did not uncover mutations specific to the nonrejected SCCs (Supplementary Fig. S1K; Supplementary Table S2; Supplementary Table Legends), suggesting that nongenetic mechanisms, such as variations in gene expression and pathways in the tumor cells or TME, accounted for the differences between rejected and nonrejected clones.

Furthermore, flow cytometry revealed that differences in MHC class I (MHC-I) and class II (MHC-II) surface levels did not explain the aggressive phenotype (Supplementary Fig. S1L). MHC-I immunopeptidomics (42) on all five SCCs and the parental cell line showed a similar antigenic landscape

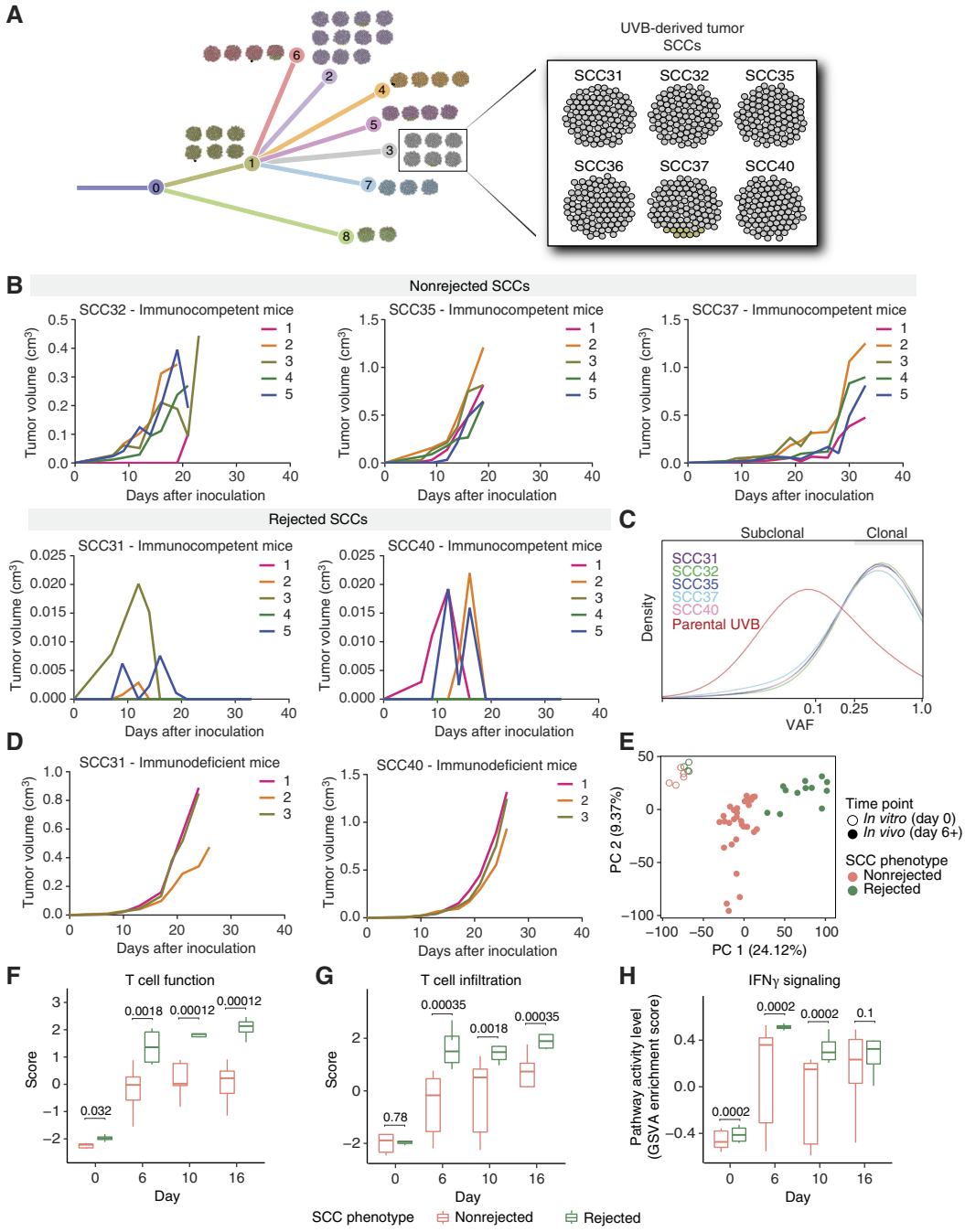

Figure 1. SCCs with the same clonality and >80% genetic similarity show opposite growth phenotypes. **A,** Phylogenetic tree representing data from the UVB-irradiated B2905 cell line. The tree depicts the results from mutation-based clustering analysis, which was used to define the distinct subclones present within the UVB cell line. The phylogenetic relationship between subclones is shown; each of the 40 UVB-derived SCCs was mapped onto the subclonal branch with the highest genetic similarity. Each of the 40 SCCs is depicted as a ball of 100 tumor cells, with the color coding reflecting the percentage frequency of each branch in each SCC sample. Top, Left boxes show the UVB sample (median and mean variant VAF) as a ball of 100 tumor cells, color-coded to match the subclonal branches. **B,** Growth curve of nonrejected (top) and rejected (bottom) SCC-derived tumors *in vivo* in immunocompetent mice. $n = 5$. **C,** VAF distribution of parental UVB-irradiated B2905 cells (red), rejected SCC31 (purple), and SCC40 (pink) cells and nonrejected SCC32 (green), SCC35 (blue), and SCC37 (light-blue) cells in the $\log_2$ space. VAF > 0.25 ($\log_2 = -2$) is considered clonal. **D,** Growth curve of rejected SCC-derived tumors *in vivo* in NSG immunodeficient mice. $n = 3$. **E,** PCA plot based on the TMM-normalized log CPM gene expression of the rejected (green) and nonrejected (pink) clones across *in vitro* (day 0; open circles) and *in vivo* (days 6, 10, 16, and 20; closed circles) time points after removing outlier samples ("Methods"). Top two PCs are shown, with the percentage of explained total variance labeled on the corresponding axis. **F,** T cell function scores and (**G**) T cell infiltration scores, both computed with the TIDE algorithm in the rejected (green) and nonrejected (pink) clones across different time points (*x*-axis). The scores between the rejected and nonrejected clones were compared with a linear model at each time point ("Methods"), and the corresponding Benjamini–Hochberg adjusted *P* values are shown. **H,** GSVA enrichment scores of the IFNγ pathway ("Methods") in the rejected (green) and nonrejected (pink) clones across different time points (x-axis). Enrichment for the IFNγ pathway genes was tested with gene set enrichment analysis ("Methods"), and the corresponding Benjamini–Hochberg adjusted *P* values are shown.

(Supplementary Fig. S2A–S2C), as well as a large overlap of the source genes between samples (Supplementary Fig. S2D and S2E). Examination of neoantigen presentation in each cell line identified three neopeptides, none of which could provide an explanation for the differences in tumor growth (Supplementary Fig. S2F–S2I). In light of these immunopeptidome analyses, we conclude that the phenotypic differences between the different tumors are unlikely because of the higher number of presented neopeptides in the rejected tumors. Bulk T cell receptor (TCR) sequencing of tumors derived from rejected, nonrejected, and the parental UVB cell line at days 6, 10, and 15 (Supplementary Fig. S2J) also showed no difference in TCR clonality between rejected and nonrejected tumors (Supplementary Fig. S2K and S2L).

Changes in the TME Immune Composition Explain Aggressive Tumor Growth in Low-ITH Tumors

To pinpoint changes in immune cell types that may explain differential aggressiveness in highly clonal tumors, the SCCs were inoculated separately into immunocompetent mice, and tumors were harvested at sequential time points (days 6, 10, and 16 after inoculation for both groups, as well as at day 20 after inoculation for the nonrejected group). Harvested tissue was dissociated for bulk RNA sequencing (RNA-seq) alongside SCC cell lines representing day 0. Gene expression levels were compared across groups to identify differentially expressed genes and enriched pathways.

Principal component analysis (PCA) revealed three well-defined clusters of expression patterns corresponding to (i) *in vitro* SCCs from day 0, (ii) *in vivo* tumors from nonrejected clones, and (iii) *in vivo* tumors from rejected clones. Gene expression differences across samples were only evident *in vivo* (Fig. 1E), in which T cell function and T cell infiltration signatures were increased in rejected tumors compared with nonrejected tumors (Fig. 1F and G), as computed by Tumor Immune Dysfunction and Exclusion (TIDE; ref. 43). Gene set enrichment analysis on differentially expressed genes in the rejected versus nonrejected groups (Supplementary Tables S3 and S4; Supplementary Table Legends) highlighted genes encoding IFNγ signaling pathway components. Specifically, *Camk2a*, *Irf1*, *Ifngr*, *Stat1*, *Jak1*, and *Jak2* were consistently enriched in rejected clones, both *in vitro* and across *in vivo* time points (Fig. 1H). IFNγ plays a central role in antitumor immunity by upregulating MHC-I expression and inducing the immunoproteasome (44). This pathway may thus affect immune responses in patients with melanoma and contribute to mouse tumor rejection.

To fully decipher differences in the TME of tumors from rejected and nonrejected SCCs, we performed single-cell RNA-seq (scRNA-seq) on tumors harvested from mice at days 0, 6, 10, 16, and 20 after inoculation. Integration of cells from all tumors and time points revealed several cell type–specific signatures and highlighted a dominant population of tumor and stromal cells expressing *Vim*, *Cd81*, and *Pcbp2* (Fig. 2A; Supplementary Fig. S3A). We also captured the immune compartment, including adaptive immune cells such as T cells (*Cd3e* and *Cd3g*) and NK cells (*Nkg7* and *Gzma*), along with myeloid populations of monocytes (*Cd14* and *Fcgr1*), macrophages (*Cd74* and *Apoe*), and dendritic cells (DCs; *H2-Eb1* and *Il1b*; Supplementary Fig. S3A). Higher proportions of macrophages were observed in nonrejected SCC-derived tumors, especially at day 10 after inoculation (Fig. 2B; Supplementary Fig. S3B).

To further investigate the distinct immune microenvironment in rejected and nonrejected tumors, we reclustered cells in the immune compartment (Supplementary Fig. S3C). This approach resolved the T cell compartment into cytotoxic CD8$^+$ T cells (*Nkg7* and *Ccl5*), CD4$^+$ Tregs (*Foxp3* and *Ctla4*), conventional CD4$^+$ T cells (*Ifng* and *Rora*), and proliferating T cells (*Mki67*; Supplementary Fig. S3D). We measured a significant decrease in CD8$^+$ and conventional CD4$^+$ T cell frequency and a higher exhaustion phenotype in the nonrejected tumors (Fig. 2C and D). Furthermore, we used *Mki67* expression to separate macrophages into resting and proliferating populations (Supplementary Fig. S3C and S3E). We found a significantly higher fraction of both populations in nonrejected tumors at day 10 after inoculation (Fig. 2E). Indeed, nonrejected tumors contained higher frequencies of proliferating macrophages by day 6. Thus, the TME of nonrejected SCCs may induce macrophage proliferation shortly after tumor formation. Reclustered analysis of the myeloid compartment also showed significant macrophage enrichment in nonrejected SCCs at days 6 and 10 after inoculation (Fig. 2E; Supplementary Fig. S3F). When we specifically analyzed CD14$^+$ monocytes and macrophages, we identified six clusters, with clusters 2 and 5 significantly enriched in nonrejected tumors (Fig. 2F and G; Supplementary Fig. S3G). These two clusters had a high M2 protumorigenic score (Fig. 2H), as well as high expression of *C1qa*, *C1qb*, *C1qc*, and *Apoe* (Fig. 2I; refs. 45–49). These data further strengthen our observation that relatively high numbers of protumorigenic macrophages accumulate in nonrejected compared with rejected SCC-derived tumors.

Next, we analyzed rejected and nonrejected tumors at days 6 and 10 after inoculation using Opal Multiplex IHC staining and CODEX multiplexed tissue imaging, respectively. These data validated the scRNA-seq results, showing significantly higher CD206$^+$CD204$^+$ protumorigenic macrophages and lower CD8$^+$ T cell infiltration in the nonrejected tumors (Fig. 3A–D; Supplementary Fig. S4A). The nonrejected SCCs also contained a significantly higher percentage of exhausted CD8$^+$ T cells, based on TIM3 and LAG3 co-expression (Fig. 3E). Furthermore, Ki67 staining indicated significantly increased proliferation of CD45$^+$ immune cells and specifically CD8$^+$ T cells in the rejected SCCs (Supplementary Fig. S4B–S4D).

Next, we measured differences in key immunologic and cell-state markers using cytometry by time of flight (CyTOF) in SCC-derived tumors. CyTOF analysis corroborated our scRNA-seq and IHC staining results, showing increased CD8$^+$ T cell infiltration in rejected tumors and increased TAMs in nonrejected tumors (Fig. 3F and G; Supplementary Fig. S5A–S5F). Furthermore, CD62L$^+$CD8$^+$ T cells were seen in rejected tumors, whereas more PD-1$^+$GzmB$^+$ CD8$^+$ T cells were identified in nonrejected tumors (Fig. 3F), indicating higher T cell exhaustion in the latter group. Furthermore, we identified more CD62L$^+$CD4$^+$ T cells in the rejected tumors than in the nonrejected tumors, which were instead enriched with PD-1$^+$CD4$^+$ T cells (Supplementary Fig. S5D). Increased levels of CD206$^+$ macrophages were found in the nonrejected tumors, specifically Ki67$^+$CD206$^+$ proliferating macrophages,

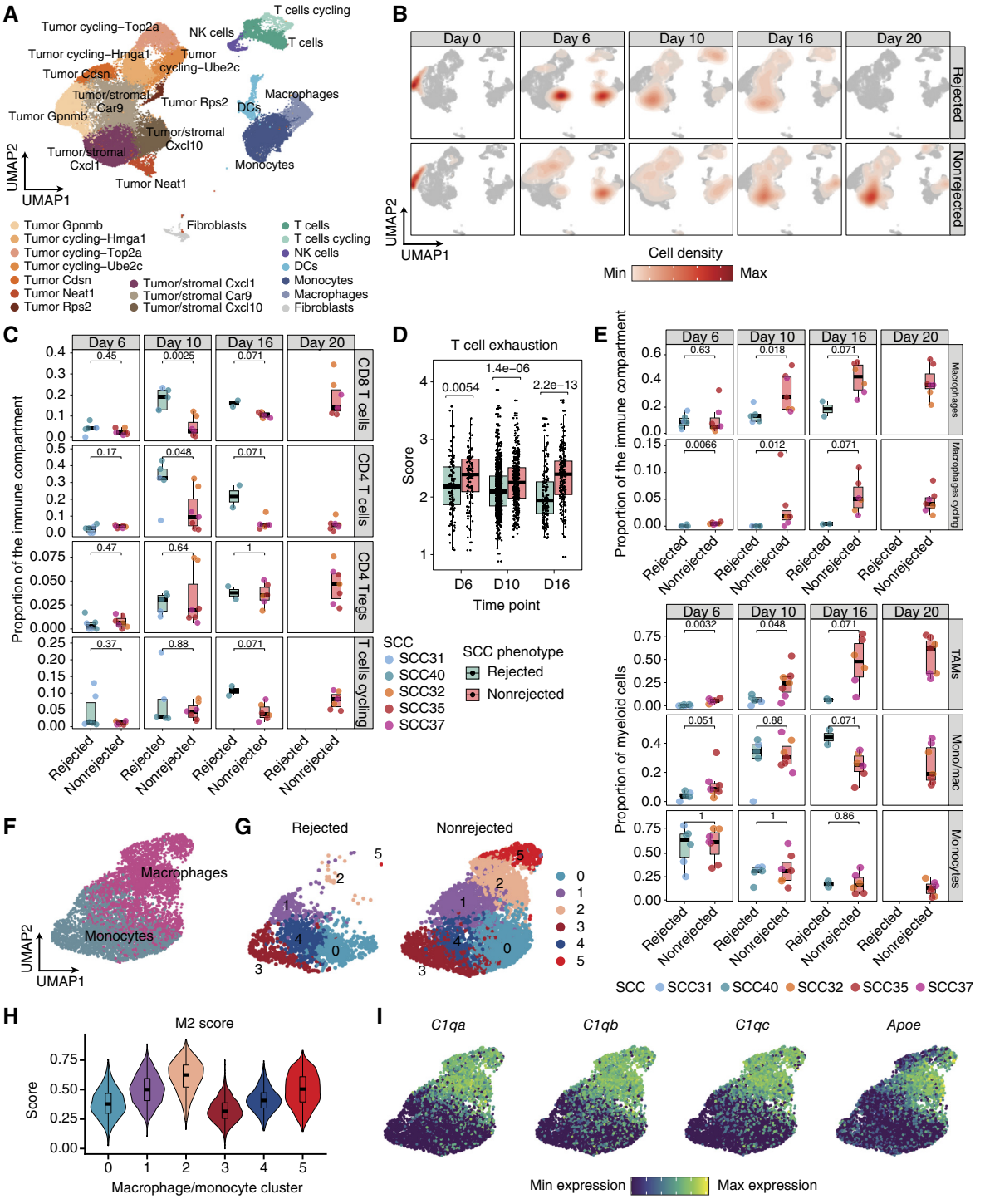

Figure 2. scRNA-seq reveals increased M2-like macrophage infiltration in nonrejected tumors. **A,** Uniform manifold approximation and projections (UMAP) of cell types obtained by analysis of scRNA-seq data from rejected and nonrejected tumors ($n = 41{,}930$ cells total). **B,** UMAP as in (**A**) overlayed with the density of all cells per SCC group (rejected or nonrejected) and time point after tumor inoculation. **C,** Boxplot of cell-type proportions within T cell clusters in the immune compartment of rejected and nonrejected SCCs on days 6, 10, 16, and 20 after tumor inoculation. Statistical testing by the two-sided Wilcoxon test. **D,** Boxplot of CD8$^+$ T cell exhaustion (104) scores in rejected (green) and nonrejected (red) tumors generated from SCCs from day 6 to day 16. The individual points denote T cell exhaustion scores of CD8$^+$ T cells across different replicates of a particular clone. *P* values were determined using the Wilcoxon test between rejected and nonrejected SCCs at different time points. **E,** Boxplot of cell-type proportions in macrophage clusters within the immune compartment (top) or myeloid compartment (bottom) of rejected and nonrejected SCCs on days 6, 10, 16, and 20 after tumor inoculation. Statistical testing by the two-sided Wilcoxon test. **F–H,** Distribution of mono/mac subclusters across rejected and nonrejected groups, with M2 scores for each subcluster ($n = 6{,}563$ monocytes/macrophages). **I,** Gene expression patterns of *C1qa*, *C1qb*, *C1qc*, and *Apoe* across different subclusters of monocytes/macrophages. Max, maximum; Min, minimum.

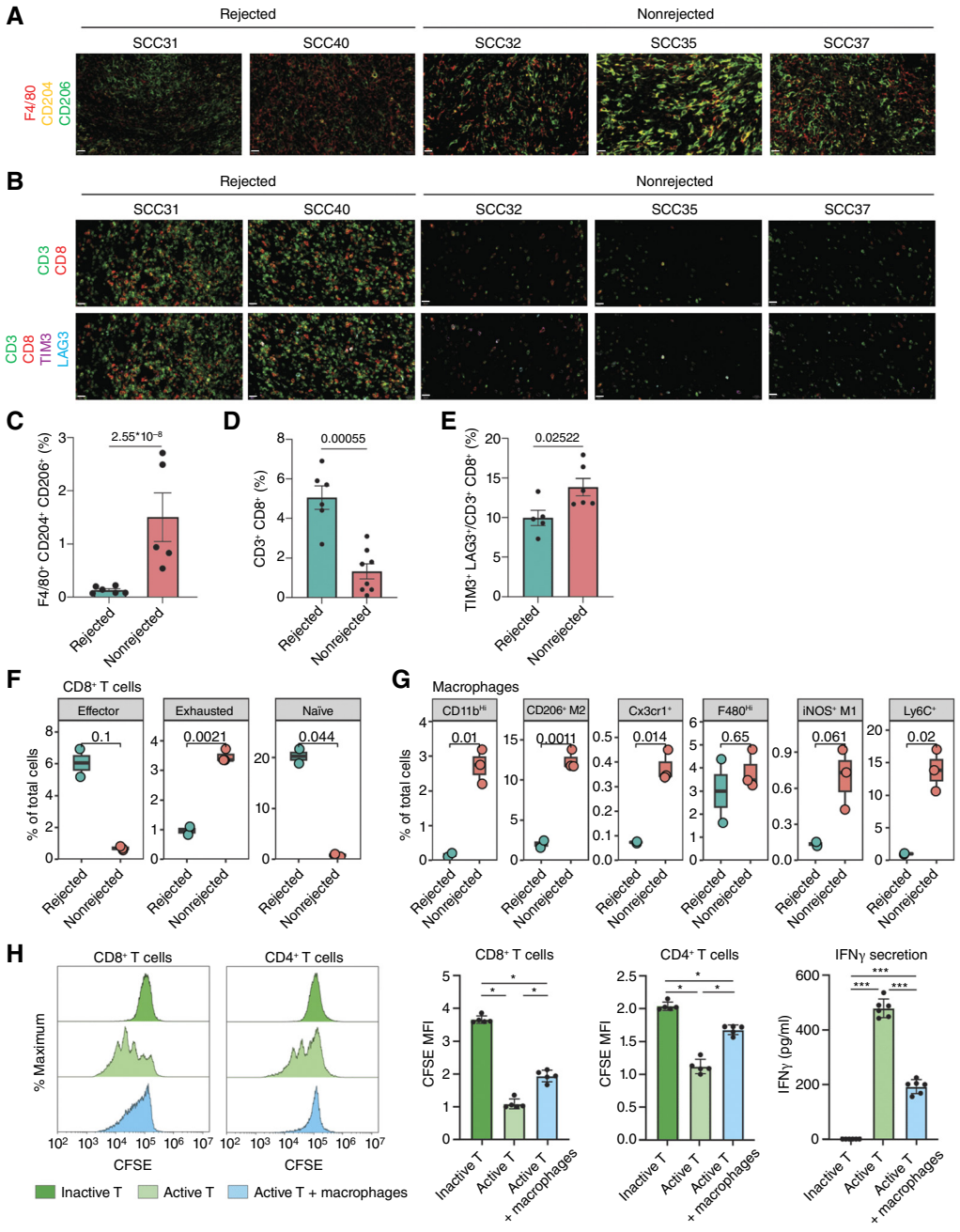

Figure 3. Opal and CODEX multiplexed tissue imaging data validate increased M2-like macrophage infiltration and T cell exhaustion in the nonrejected SCCs. **A,** Representative Opal Multiplex IHC stains for F4/80 (red), CD204 (yellow), and CD206 (green) in tumors derived from SCC31, SCC40, SCC32, SCC35, and SCC37 on day 10 after inoculation. Four areas from each tumor and three tumors from each SCC were examined. Scale bars, 20 μm. DAPI staining is not shown. **B,** Representative CODEX multiplexed tissue images for CD3 (green), CD8 (red), TIM3 (magenta), and LAG3 (cyan blue) in tumors derived from SCC31, SCC40, SCC32, SCC35, and SCC37 on day 6 after inoculation. Five areas from each tumor and three tumors from each SCC were examined. Scale bars, 20 μm. **C,** Quantification of the percentage of $F4/80^+CD204^+CD206^+$ cells described in **A**. Data are mean ± SEM. The rejected and nonrejected groups were compared using the Wilcoxon rank-sum test; $W = 456$; $P = 2.55 \times 10^{-8}$. **D,** Quantification of the percentage of $CD3^+CD8^+$ cells described in **B**. Data are mean ± SEM. $P = 0.00055$; $t = -5.27$; degrees of freedom (df) = 9, unpaired t test. **E,** Quantification of the percentage of $TIM3^+LAG3^+/CD3^+CD8^+$ cells described in **B**. Data are mean ± SEM. $P = 0.02522$; $t = 2.6798$; df = 9, unpaired t test. **F,** Boxplot quantifying the percentage of total cells for each CD8 cluster identified in CyTOF analysis. **G,** Boxplot quantifying the percentage of total cells for each macrophage cluster identified in CyTOF analysis. **H,** CFSE-based T cell proliferation assay after co-culture for 48 hours with nonrejected SCC35 tumor-derived macrophages isolated 10 days after inoculation. Representative histogram plot and quantification of CFSE intensity ($n = 5$). $CD8^+/CD4^+$ T cells isolated from healthy mouse spleens cultured without macrophages served as the controls. CD8: Kruskal–Wallis χ^2 test, $\chi^2 = 12.5$; $P = 0.001930454$. Pairwise comparison by the Wilcoxon test with Bonferroni correction is shown in the figure. *, P value < 0.05. CD4: Kruskal–Wallis χ^2 test, $\chi^2 = 12.5$; $P = 0.00193$. Pairwise comparison by the Wilcoxon test with Bonferroni correction is shown in the figure. *, P value < 0.05. ELISA measurement of IFNγ in culture media 48 hours after co-culture of T cells with or without tumor-derived macrophages. $n = 6$. Data are mean ± SEM. Kruskal–Wallis χ^2 test, $\chi^2 = 15.726$; $P = 0.0003847$. Pairwise comparison by the Wilcoxon test with Bonferroni correction is shown. ***, P value < 0.01. MFI, mean fluorescence intensity.

verifying the higher TAM infiltration found above (Fig. 3G; Supplementary Fig. S5E). Increased levels of DCs infiltrated the rejected tumors, as observed by scRNA-seq (Supplementary Fig. S5F).

Importantly, co-culturing nonrejected SCC tumor-derived macrophages with carboxyfluorescein diacetate succinimidyl ester (CFSE)–labeled $CD8^+$ or $CD4^+$ T cells from naïve mouse spleens inhibited T cell proliferation. Furthermore, nonrejected SCC tumor-derived macrophages significantly lowered IFNγ secretion from T cells, indicating decreased cytotoxic activity (Fig. 3H; Supplementary Fig. S5G). These findings argue that macrophages infiltrate highly aggressive tumors and suppress T cell function, facilitating tumor immune escape.

scRNA-seq Identifies Core Rejection and Nonrejection Signatures That Stratify Patient Survival

Next, we examined tumor-intrinsic factors that influence the dramatic differences in immune cell composition in nonrejected versus rejected SCC-derived tumors. Although all tumor populations shared a core identity, expressing genes such as *Vim*, *Gpx4*, and *Pcbp2* (Supplementary Fig. S3A), we found numerous transcriptional differences between the aggressive and nonaggressive tumors. We examined differential gene expression in the tumor compartment of nonrejected versus rejected clones at each time point (days 0, 6, 10, and 16 after inoculation). A total of 128 genes were differentially expressed at day 0 (101 upregulated in nonrejected and 27 upregulated in rejected clones), 282 genes at day 6 (123 in nonrejected and 159 in rejected clones), 169 genes at day 10 (79 in nonrejected and 90 in rejected clones), and 204 genes at day 16 (100 in nonrejected and 104 in rejected clones; fold change >1.5; Bonferroni-corrected P value < 0.01, Wilcoxon rank-sum test; Supplementary Table S5; Supplementary Table Legends; "Methods").

To define shared transcriptional programs associated with tumor aggressiveness, we identified core gene sets that were upregulated in either all rejected or all nonrejected clones at each time point. This revealed 4, 11, and 13 core genes that were overexpressed in both rejected clones at days 0, 6, and 10, respectively (Supplementary Fig. S6A). Additionally, 29, 13, and 11 core nonrejection genes were expressed at days 0, 6, and 10, respectively (Supplementary Fig. S6B). Notably, all day 0 nonrejected clones expressed higher levels of calreticulin, protein isomerase *Pdia3*, and members of the S100 protein family (*S100a4* and *S100a6*), which are genes associated with tumor progression and increased metastasis (50).

Next, we tested whether core gene sets from days 0 and 6 (Supplementary Fig. S6A and S6B) can stratify patients with high/low ITH and patients with hot/cold tumor annotations. On days 0 and 6 (log-rank test, P value = 0.014 and 0.04, respectively), core gene sets significantly stratified patients with high/low ITH in TCGA by survival. Low ITH and high expression of the rejection-related gene sets were associated with higher survival probability (Supplementary Fig. S7A and S7B). Similarly, on days 0 and 6, core gene sets significantly stratified patients in TCGA with hot versus cold tumors according to survival. A higher expression of the nonrejection-related gene sets was associated with poor survival for patients with cold tumor at day 0 (P value = 0.0014), and higher expression of the rejection-related gene set was associated with better survival for patients with hot tumor at day 6 (P value = 0.0037; Supplementary Fig. S7C and S7D).

Mif Is Overexpressed in Nonrejected Clones and in Patients with Melanoma with Poor Survival

Next, we searched for genes that were consistently differentially expressed in clones across time points. A total of 78 genes were upregulated in rejected clones at two or more time points, including the arginine metabolism enzyme *Ass1*, which has been linked to tumor suppression and better patient prognosis in breast cancer and hepatocellular carcinoma (Fig. 4A; ref. 51). In total, 91 genes were upregulated in nonrejected tumors at two or more time points, including macrophage migration inhibitory factor (*Mif*), *Lgals1*, and *S100a11* (Fig. 4A). As these genes were consistently upregulated in nonrejected SCCs, we hypothesized that they may mediate tumor aggression.

To rationally choose the best targets for further exploration, we performed an *in vivo* CRISPR screen to identify genes required for immune evasion. To this end, we created a pooled CRISPR single-guide RNA (sgRNA) library targeting 200 genes that were differentially expressed in the nonrejected tumors at days 0, 6, 10, or 16 after inoculation. We also included five nontargeting control guides and a set of three depletion (e.g., *Cd47*) and two enrichment control (e.g., *Pten*) genes, based on a previous study (52). We transduced the nonrejected SCC35 cell line with the sgRNA library and Cas9 using selective CRISPR antigen removal (SCAR) lentiviral vectors to induce per-cell knockouts (KO) *in vitro*, while avoiding immune-mediated rejection of CRISPR–Cas9 components *in vivo* (Fig. 4B; refs. 53, 54). The edited SCC35 cell lines were split into three replicates at day 0 and sequenced to verify high sgRNA recovery rates, which ranged from 93.5% to 95.6% of the original guide library (Supplementary Fig. S8A).

These input pools were inoculated into immunocompetent mice. Tumors were then harvested, dissociated, and subjected to sgRNA-seq on day 20 after inoculation (Fig. 4B; Supplementary Fig. S8B). At day 20, we recovered between 40.6% and 73.6% of sgRNAs in the pooled library, a decrease relative to the day 0 input library, likely reflecting *in vivo* selection pressures (Supplementary Fig. S8A). Guide enrichment/depletion was assessed in the day 20 library compared with the day 0 library using a negative binomial model ("Methods"). We identified 451 significantly depleted and 397 significantly enriched guides, and 33 significantly depleted genes and 38 significantly enriched genes (FDR-adjusted P value < 0.05, absolute log fold change >1). We recovered all four guides targeting *Pten*, one enrichment control, at day 20 in both replicates M4 and M5 (4/4 guides significantly enriched at adjusted P value < 0.05 in M4; 2/4 guides significant in M5; Fig. 4C; Supplementary Fig. S8C and S8D). Furthermore, guides targeting one depletion control, *Cd47*, were depleted in all replicates at the guide level (4/4 guides depleted in M3; 4/4 in M4; 3/4 in M5) and at the gene level (adjusted P value = 0.000171 in M4). Thus, our pooled screen recapitulated known effects of gene KOs on tumor aggressiveness. Indeed, the most strongly depleted guide in the entire CRISPR

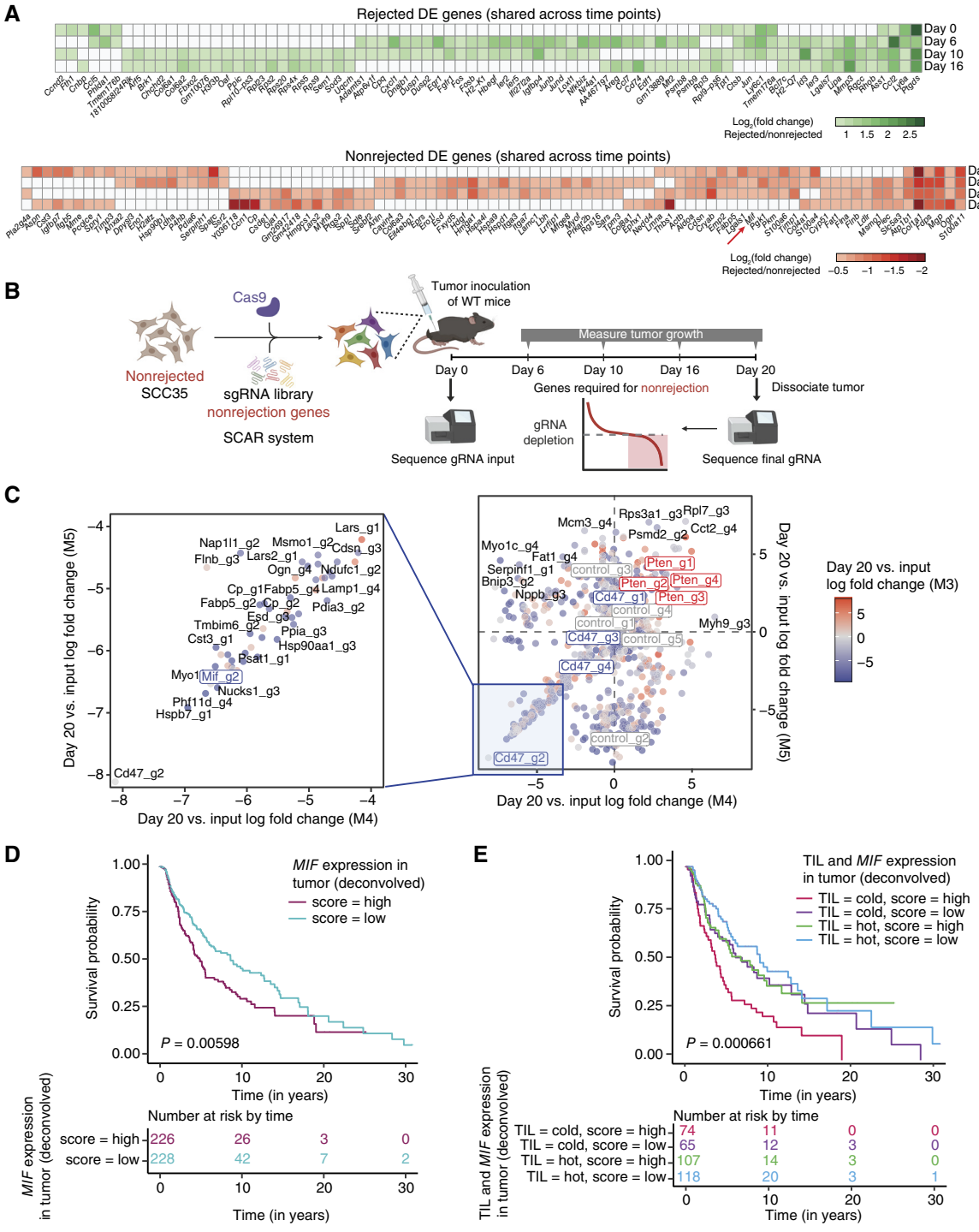

Figure 4. *Mif* is overexpressed in nonrejected clones and in patients with melanoma with poor survival. **A,** Genes that are consistently differentially expressed across several time points in rejected (top) compared with nonrejected (bottom) clones based on scRNA-seq analysis. *Mif* is differentially expressed in the nonrejected clones at 3 time points. **B,** Schematic of pooled *in vivo* CRISPR screen for nonrejection genes. **C,** sgRNA depletion and enrichment of CRISPR-edited libraries. The score represents the average log fold change of guide counts at day 20 after inoculation and day 0 input libraries, for the indicated replicates (M3, M4, M5). Highlighted in the left square are the top depleted guides. **D,** Kaplan–Meier survival curves (time in years on the *x*-axis) of deconvolved gene expression (57) in patients with melanoma in TCGA stratified by estimated *MIF* expression in tumor cells (*MIF* high for 226 and *MIF* low for 228 patients). *P* values were determined using the log-rank test to compare the overall survival probability between patients with high (red) and low (blue) estimated *MIF* expression. **E,** Kaplan–Meier survival curves (time in years on the *x*-axis) of deconvolved gene expression (57) in patients with melanoma in TCGA stratified by four mutually exclusive combinations of (i) TIL patterns based on pathologic annotation of tumors as being hot or cold in Saltz and colleagues (58) and (ii) deconvolved *MIF* expression in tumor cells as (TIL = cold, MIF = high: 74; TIL = cold, MIF = low: 65; TIL = hot, MIF = high: 107; and TIL = hot MIF = low: 118). *P* values were determined using the log-rank test to compare the overall survival probability between patients with combinations of hot/cold patterns and high/low estimated *MIF* expression.

screen for replicates M4 and M5 was Cd47_g2 (M4: log fold change −8.12, FDR-adjusted *P* value = 0.02; M5: log fold change −8.11, FDR-adjusted *P* value = 0.02; Fig. 4C; Supplementary Fig. S8C).

A guide targeting *Mif* was strongly depleted (Mif_g2; M4: log fold change −6.31, FDR-adjusted *P* value = 0.05; M5: log fold change −6.24, FDR-adjusted *P* value = 0.05; Fig. 4C). Indeed, *Mif* expression was also consistently enriched in nonrejected clones from days 0 to 10 after inoculation (Fig. 4A). Additionally, *Mif* was significantly depleted at the gene level in replicate M4 (median log fold change −2.5, FDR-adjusted *P* value = 0.0099, Supplementary Fig. S8D).

MIF is a secreted protein that binds to the CD74 receptor, which is highly expressed on professional antigen-presenting cells such as macrophages and DCs (55). As tumor cells secrete MIF, we hypothesized that it may recruit CD74$^+$ monocytes and promote differentiation into protumorigenic macrophages, supporting an immunosuppressive environment and tumor growth (56). This hypothesis is consistent with increased infiltration of TAMs with a high M2 score and high *C1q* and *Apoe* expression in nonrejected tumors observed by scRNA-seq (Fig. 2E–I). To test this hypothesis, we performed CellPhoneDB analysis to infer the cross-talk between cell types in our data. Indeed, one of the top interactions was between MIF in tumor cells and CD74 in macrophages and monocytes (Supplementary Fig. S9A). Comparing the top pairs from the CellPhoneDB analysis with differentially expressed genes revealed that *Mif* came up across time points in both analyses in nonrejected clones (Supplementary Fig. S9B).

We also performed CellChat analysis to infer differences in cell–cell signaling pathways. Comparing rejected versus nonrejected cell–cell communication at each time point revealed increased MIF signaling in nonrejected clones at days 6 and 10, predominantly from tumor cells to macrophages (Supplementary Fig. S9C–S9F). To verify that tumor cells are the dominant source of MIF signaling, we evaluated *Mif* expression among the clusters identified by scRNA-seq (Fig. 2A). Although *Mif* was expressed in many cell types, its expression was highest in tumor clusters, even when compared with stromal cells [as inferred by copy-number variation (CNV) analysis, Supplementary Fig. S10A–S10C; "Methods"].

To assess the relevance of our mouse data to human melanoma, we examined patient tumor samples using Opal Multiplex IHC staining. To examine MIF in specific immune subsets in the TME, we used three tissue microarrays (TMA) containing melanoma tumors, annotated as immune-inflamed, immune-excluded, and immune-deserted based on their T cell infiltration level. We stained the TMAs for MIF, T cells (CD3), and M2 macrophages (CD163 and CD68) and evaluated their levels. Biopsies associated with high T cell infiltration (immune-inflamed) showed the largest percentage of CD3$^+$ cells. Cases lacking T cell infiltration (immune-deserted) were associated with the lowest percentage of CD3$^+$ values, validating our mouse T cell staining. Immune-deserted samples were also associated with the largest percentage MIF$^+$ signal and *vice versa*, showing an opposite trend to CD3$^+$ values. High MIF$^+$ tumors were correlated with increased TAM infiltration, consistent with mouse scRNA-seq and supporting the relevance of our mouse data in patient samples (Supplementary Fig. S11A–S11D).

We examined estimated *MIF* expression and tumor aggressiveness across 11 different cell types by analyzing deconvolved cell type–specific expression data from TCGA datasets of patients with melanoma [deconvolution done with CODEFACS (57); Supplementary Fig. S12A]. This analysis revealed significantly poorer survival of patients estimated to express high versus low *MIF* levels in tumor cells (Fig. 4D; log-rank test, $P = 0.00598$). Interestingly, we also observed significantly poorer survival of patients with high estimated *MIF* expression in stromal cells, including endothelial cells (Supplementary Fig. S12B; log-rank test, $P = 0.0943$) and fibroblasts (Supplementary Fig. S12C; log-rank test, $P = 0.335$). Importantly, we also analyzed deconvolved gene expression data from melanomas annotated as having a tumor-infiltrating lymphocyte (TIL) pattern (Supplementary Fig. S12D; log-rank test, $P = 1.5e{-}09$; ref. 58). This analysis accentuated poorer survival for patients bearing both cold tumors and high estimated *MIF* expression in tumor cells than those with cold tumors and low *MIF* expression (Fig. 4E; log-rank test, $P = 0.000661$). Our analysis further highlights *MIF*/*Mif* as a possible factor that underlies immune escape by nonrejected clones.

Mif KO in Aggressive Clones Significantly Reduces Tumor Growth

To assess whether *Mif* contributes to aggressive tumor growth in mice, we knocked out *Mif* using the CRISPR–Cas9 system in both nonrejected SCC35 (KO clones 19 and 24) and SCC37 (KO clone 21; Supplementary Fig. S13A). *Mif* KO clones showed similar proliferation rates to parental *Mif* wild-type (WT) cells *in vitro* (Supplementary Fig. S13B), arguably because *Mif* loss did not reduce the baseline growth rate. Injecting these KO clones into immunocompetent mice gave rise to significantly smaller tumors than with parental *Mif* WT or control cells, which were transfected with the same CRISPR–Cas9 vectors, sorted for GFP$^+$ phenotype, grown as SCCs, but found to have *Mif* WT by Sanger sequencing (Fig. 5A; Supplementary Fig. S13C).

To investigate the effect of *Mif* clonality on tumor growth, we injected immunocompetent mice with seven mixtures of *Mif* KO and *Mif* WT cells at different ratios and monitored tumor growth. When *Mif* was expressed in ≥50% of the tumor cells, tumors grew rapidly (Supplementary Fig. S13D). Conversely, when *Mif* clonality was low (<25%), tumors did not grow to large volumes, arguing that *Mif* clonality is a key factor mediating tumor growth and denoting MIF expression as a potential biomarker for tumor aggressiveness. Our data suggest that below a certain threshold with a low number of cells expressing *Mif*, tumor growth is nonaggressive. To validate these experimental findings using patient data, we examined the survival probability of patients with varying *MIF* expression subdivided into four quartiles (Supplementary Fig. S13E). The survival probability of patients with melanoma in TCGA decreased gradually from the lower to higher quartiles of deconvolved *MIF* expression in tumor cells. The survival probability is significantly higher for patients with *MIF* expression in the lowest quartile than for patients with *MIF* expression in the higher third or fourth quartile (Supplementary Fig. S13E).

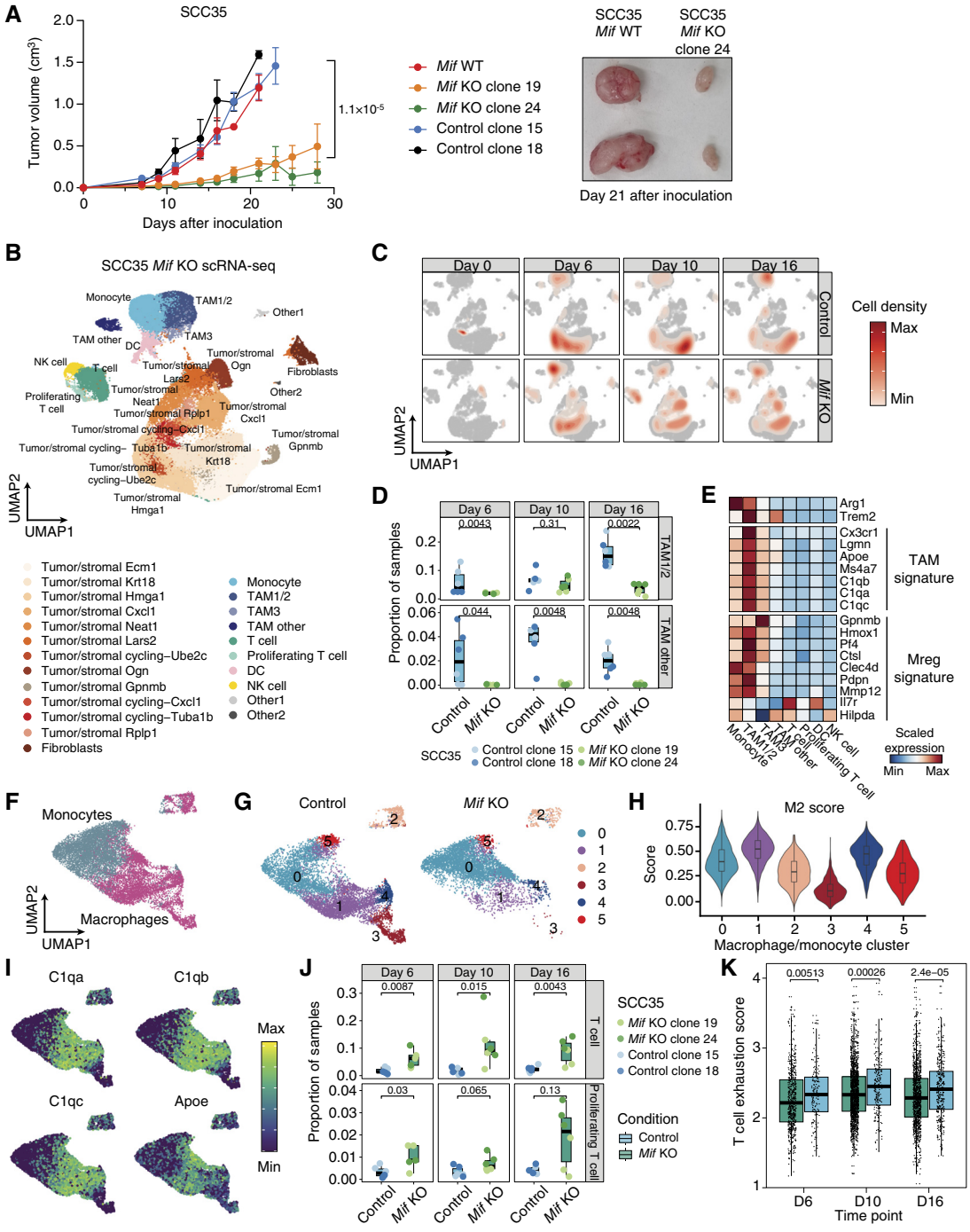

Figure 5. Decreased macrophage and increased T cell infiltration of SCC-derived tumors with *Mif* KO. **A,** *Mif* KO using CRISPR in nonrejected SCC35 significantly decreased tumor growth. $n = 3$–5. On day 21 after inoculation, the Kruskal–Wallis χ^2 test shows χ^2 (degrees of freedom = 4) 15.392; $P = 0.0039$. Pairwise comparison by the Wilcoxon test comparing *Mif* WT clones with *Mif* KO clones found a significant difference ($P = 1.1 \times 10^{-5}$). **B,** Uniform manifold approximation and projections (UMAP) of cell types based on scRNA-seq data from SCC35-derived tumors with or without *Mif* KO. Data show samples from all tumors and time points aggregated together ($n = 85{,}952$ cells total). **C,** UMAP as in (**B**) overlayed with the cell density of all cells per condition (control or *Mif* KO) and time point after tumor injection. **D,** Boxplot of cell-type proportions in macrophage clusters from control and *Mif* KO clones at days 6, 10, 16, and 20 after tumor inoculation. Statistical testing by the two-sided Wilcoxon test. **E,** Heatmap of TAM markers among immune cell-type clusters. **F** and **G,** Distribution of monocyte/macrophage subclusters between *Mif* KO and control groups ($n = 14{,}576$ monocyte/macrophage cells). **H,** M2 score for each subcluster of monocytes/macrophages. **I,** Expression of *C1qa*, *C1qb*, *C1qc*, and *Apoe* genes across different subclusters of monocytes/macrophages. **J,** Boxplot of cell-type proportions in T cell clusters from control and *Mif* KO clones at days 6, 10, 16, and 20 after tumor inoculation. Statistical testing by the two-sided Wilcoxon test. **K,** Boxplot of general T cell exhaustion (104) scores between *Mif* KO (green) and control (blue) tumors generated from SCC35 from day 6 to day 16 (legend as in **J**). Individual points denote the T cell exhaustion scores of T cells across different replicates of a particular clone. *P* values were determined using the Wilcoxon test between rejected and nonrejected tumor cells at different time points. Mreg, regulatory macrophages; Max, maximum; Min, minimum.

Next, we assessed whether the TME of *Mif* KO SCC-derived tumors exhibited changes compared with tumors established from nonrejected SCCs. We performed scRNA-seq on tumors from SCC35-derived *Mif* KO clones and control SCC35 tumors at days 0, 6, 10, and 16 after inoculation. Integrating data from all time points and clones revealed that the range of cell types observed broadly recapitulated our scRNA-seq data from rejected versus nonrejected SCCs (Figs. 2A and 5B). More specifically, we captured a large population of tumor/stromal cells, while the immune compartment was composed of macrophages, monocytes, DCs, NK cells, and T cells in both resting and proliferating states (Fig. 5B). We confirmed that *Mif* expression was indeed lower among tumor cells in *Mif* KO clones than in control clones (Supplementary Fig. S13F).

To examine the differences in transcriptional profiles between the *Mif* KO and control clones, we performed a differential expression (DE) analysis of the tumor compartment between the two conditions at each time point (days 0, 6, 10, and 16 after tumor inoculation). As expected, *Mif* was one of the most downregulated genes in the *Mif* KO tumor cells at all time points (Supplementary Fig. S13G). The *Mif* KO tumor cells upregulated inflammatory genes such as *Stat1*, *Ifi27l2a*, and *Cxcl10* at multiple time points. We performed gene set enrichment analysis of differentially expressed genes in *Mif* KO tumor cells using the Molecular Signatures Database hallmark gene sets. *Mif* KO tumor cells upregulated IFN signaling and inflammatory response pathways (Supplementary Fig. S13H), suggesting that *Mif* KO in nonrejected SCC35 pushes transcriptional states toward that of rejected tumor clones.

Unsupervised hierarchical clustering of pseudobulked tumor samples from rejected, nonrejected, *Mif* KO, and control clones at days 0, 6, 10, 16, and 20 (Supplementary Fig. S14A and S14B) revealed that nonrejected SCCs clustered together with the control samples (which also express *Mif*), whereas the rejected SCCs clustered with the *Mif* KO samples. To further investigate whether the *Mif* KO tumors resemble rejected tumors, we evaluated the expression of core rejection and nonrejection signatures (Supplementary Fig. S6) in the *Mif* KO tumors. *Mif* KO tumors expressed lower levels of the core nonrejected signature at day 6 and higher levels of the core rejected signature (Supplementary Fig. S14C), arguing that *Mif* KO tumors resemble rejected tumors and that *Mif* enhances tumor growth and immune escape in low-ITH tumors.

Next, we examined TAMs in *Mif* KO clone–derived tumors and observed decreased infiltration when compared with the controls (average frequencies of TAM1/2 at day 6: 2.0% *Mif* KO, 5.9% control, Wilcoxon P value = 0.0043; at day 10: 4.7% *Mif* KO, 6.8% control, Wilcoxon P value = 0.31; and at day 16: 3.5% *Mif* KO, 16.0% control, Wilcoxon P value = 0.0022; Fig. 5B–D). These TAMs exhibited a high M2 score and *C1qa*, *C1qb*, *C1qc*, and *Apoe* expression (Fig. 5E–I; Supplementary Fig. S14D). Conversely, the myeloid population in the *Mif* KO clones was skewed toward the monocyte cluster (Fig. 5C). The increased abundance of TAMs with high expression of *C1qa*, *C1qb*, *C1qc*, and *Apoe* observed in macrophage clusters 1 and 4 (Fig. 5I) in the control when compared with *Mif* KO tumors is consistent with our finding that TAMs with a high expression of *C1qa*, *C1qb*, *C1qc*, and *Apoe* (clusters 2 and 5 in Fig. 2G–I) are more abundant in nonrejected tumors. We also found that *Mif* KO samples exhibited higher T cell infiltration than did the controls (average frequencies of T cells at day 6: 7.3% *Mif* KO, 2.0% control; at day 10: 12.3% *Mif* KO, 2.2% control; and at day 16: 10.7% *Mif* KO, 2.8% control; Fig. 5J).

To further characterize the differences in T cell infiltration induced by *Mif* KO, we reclustered the T cell populations (Supplementary Fig. S14E). This separated T cells into a naïve/memory cluster characterized by *Ccr7* and *Tcf7* expression, and two clusters of CD4$^+$ T cells differentiated by *Foxp3* expression (Supplementary Fig. S14E and S14F). We identified two clusters of CD8$^+$ T cells expressing cytotoxicity markers, including *Gzma*, *Gzmb*, and *Nkg7*, that were separated based on the expression of the proliferation marker *Mki67* (Supplementary Fig. S14F). We also captured a cluster of T cells expressing high levels of IFN-stimulated genes such as *Ifit1* and *Isg15*. By comparing these populations between conditions, we observed a higher frequency of cytotoxic CD8$^+$ T cells in *Mif* KO clones as early as at day 6 after inoculation (4.7-fold increase at day 6; 3.0-fold increase at day 10, and 9.8-fold increase at day 16; Supplementary Fig. S14G). Furthermore, the frequency of CD8$^+$ T cells increased over time in the *Mif* KO clones and stayed relatively constant in controls (Supplementary Fig. S14G). We also observed a higher frequency of Tregs in the controls by day 16 after inoculation (Supplementary Fig. S14G). These differences in T cell composition were accompanied by a lower T cell exhaustion signature in *Mif* KO clones (Fig. 5K).

To validate these findings, Opal Multiplex IHC staining and CODEX multiplexed tissue imaging were performed on samples from *Mif* WT or KO SCC35-derived tumors on day 10 after inoculation. Our data revealed decreased CD206$^+$CD204$^+$ macrophage (Fig. 6A and B; Supplementary Fig. S15A) and increased CD8$^+$ T cell infiltration into the KO tumors (Fig. 6C and D; Supplementary Fig. S15A). In addition, the CD8$^+$ T cells infiltrating the *Mif* KO tumors were significantly less exhausted and characterized by decreased LAG3 and TIM3 expression (Fig. 6C and E; Supplementary Fig. S15B–S15D).

CyTOF staining of tumors derived from *Mif* KO and *Mif* WT cells revealed that *Mif* KO tumors were infiltrated by more CD8$^+$ T cells (Supplementary Fig. S15E and S15F), corroborating our scRNA-seq, IHC staining, and CODEX data. Specifically, *Mif* KO tumors had more CD62L$^+$CD44$^+$CD8$^+$ T cells and more PD-1$^+$GzmB$^+$ exhausted CD8$^+$ T cells were identified in *Mif* WT tumors, indicating a higher T cell exhaustion phenotype in *Mif* WT tumors, thus validating insights from our scRNA-seq data. Furthermore, we identified significantly more Ki67$^+$ proliferating CD4$^+$ Treg cells in *Mif* WT than in *Mif* KO tumors (Supplementary Fig. S15E and S15G). Moreover, CD206$^+$ macrophages, and specifically Ki67$^+$ CD206$^+$ proliferating macrophages, were significantly elevated in *Mif* WT tumors, verifying the higher TAM infiltration found in the experiments above (Supplementary Fig. S15E and S15H). Increased levels of DCs infiltrated the *Mif* KO tumors, a result that was also observed in scRNA-seq analysis (Supplementary Fig. S15E and S15I).

To examine how CD8$^+$ T cell–mediated antitumor immunity affects the growth of *Mif* KO tumors, mice were inoculated with *Mif* KO clones (SCC35 KO clone 24 and SCC37 KO clone 21) after CD8$^+$ depletion. For both clones, the depletion

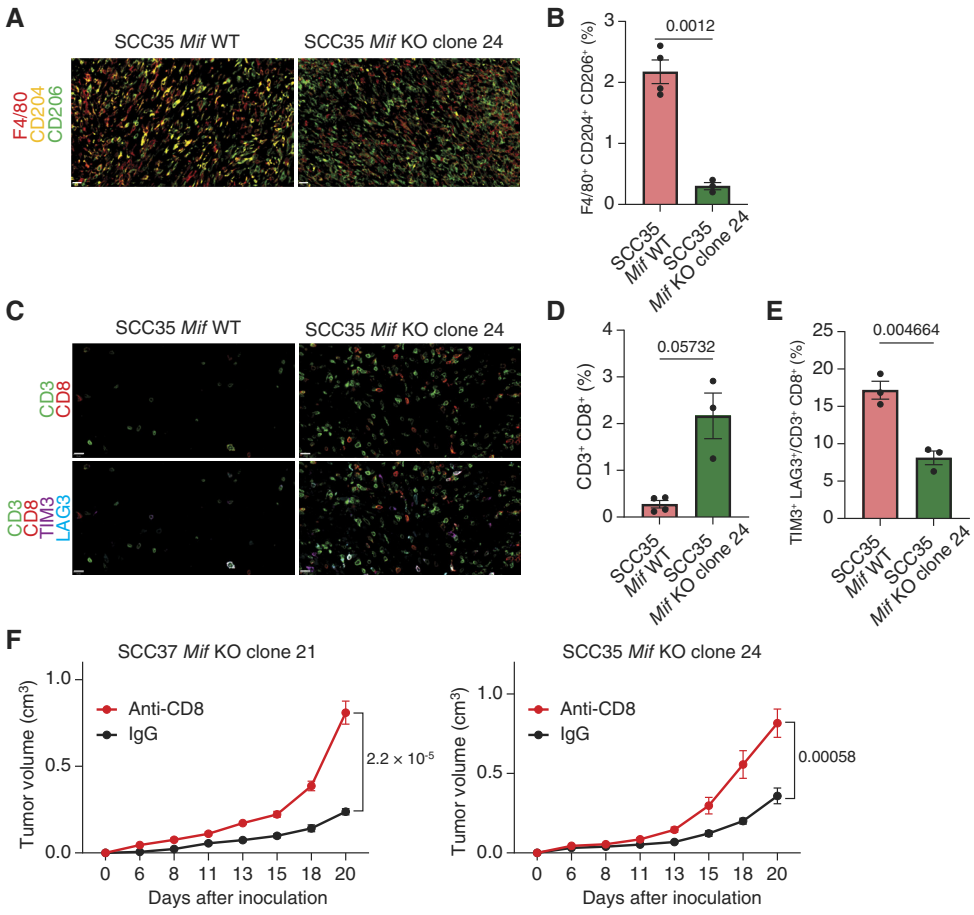

Figure 6. The decreased growth of *Mif* KO tumors is mediated by CD8⁺ T cells characterized by less exhaustion and high proliferation. **A,** Representative Opal Multiplex IHC stains for F4/80 (red), CD204 (yellow), and CD206 (green) in tumors derived from *Mif* WT or KO SCC35 on day 10 after inoculation. Four areas from each tumor and three tumors from each SCC were examined. Scale bars, 20 μm. DAPI staining is not shown. **B,** Quantification of the percentage of F4/80⁺CD204⁺CD206⁺ cells described in **A**. Data are mean ± SEM. $P = 0.0012$; $t = -10.411$; degrees of freedom (df) = 3.28, unpaired *t* test. **C,** Representative CODEX multiplexed tissue images for CD3 (green), CD8 (red), TIM3 (magenta), and LAG3 (cyan blue) in tumors derived from *Mif* WT or KO SCC35 on day 10 after inoculation. Five areas from each tumor and three and four tumors from *Mif* KO and *Mif* WT, respectively, were examined. Scale bars, 20 μm. **D,** Quantification of the percentage of CD3⁺CD8⁺ T cells described in **C**. Data are mean ± SEM. $P = 0.05732$; $t = 3.8252$; df = 4, unpaired *t* test. **E,** Quantification of the percentage of TIM3⁺ LAG3⁺/CD3⁺CD8⁺ T cells described in **C**. Data are mean ± SEM. $P = 0.004664$; $t = -6.0229$; df = 3.759, unpaired *t* test. **F,** Growth curve of tumors derived from *Mif* KO clones (left: SCC37 KO clone 21; right: SCC35 KO clone 24) in immunocompetent mice, treated with anti-CD8 antibody or IgG control. $n = 8–9$. Pairwise comparisons using the Wilcoxon rank-sum test. $P = 2.2 \times 10^{-5}$ and 0.00058, respectively.

of CD8⁺ T cells abolished the tumor-rejecting effects seen in *Mif* KO tumors, resulting in increased tumor growth (Fig. 6F; Supplementary Fig. S16A–S16C).

Altogether, these data support our hypothesis that *Mif* expression and function play a central role in inducing TAM infiltration followed by T cell dysfunction, both contributing to the immunosuppressive microenvironment and, ultimately, aggressive tumor growth.

DISCUSSION

In this study, we established an experimental system for the controlled study of factors that affect tumor aggressiveness in genetically homogeneous tumors. We established cell lines derived from SCCs that were deeply annotated genetically, establishing their mutational landscape, clonality, and phylogenic relationships. This approach allowed a comparative analysis of rejection-associated gene expression signatures. We validated our findings using *in vivo* CRISPR KO screens to assess promising candidates that might influence tumor aggressiveness, antitumor immunity, and tumor growth. Our findings in mice suggest that *Mif* expression is an important determinant of aggressive tumor growth in low-ITH tumors in melanoma.

Mif activity increased TAM frequency and decreased cytotoxic T cell infiltration into the TME. Infiltrating TAMs are protumorigenic, leading to elevated expression of complement *C1q* subunits along with *Apoe* (49, 59). These genes are overexpressed in TAMs in various tumor types, including melanoma, and are generally associated with immunosuppression and poor prognosis (45, 47, 60). IHC staining localized TAMs to the tumor core, revealing high levels of CD206⁺CD204⁺ macrophages and corroborating reports that these cell types are frequently found in patients bearing aggressive tumors

with poor survival in cancers including melanoma (61–67). Supporting this observation, patient data reveal that higher TAM infiltration correlates with worse prognosis across cancers (68), is accompanied by increased $CD8^+$ T cell exhaustion, and is connected to increased Treg numbers in the TME (49). Indeed, our scRNA-seq data revealed reduced T cell infiltration and function along with a high exhaustion phenotype, which was confirmed using CODEX multiplexed tissue imaging and CyTOF.

Our comprehensive genomic analysis sought to pinpoint mechanisms underlying these immune microenvironment phenotypes. Temporal analysis and CRISPR perturbation of differentially expressed genes shared by cancer cells in nonrejected tumors confirmed that *Mif* is critical for tumor immune evasion. Our results revealed significantly and consistently higher *Mif* expression in nonrejected than in rejected tumors throughout tumor evolution, starting from the *in vitro* day 0 samples. Unequivocal evidence that *Mif* mediates an aggressive growth phenotype came from *Mif* KOs in nonrejected SCCs; such *Mif* KO SCCs did not develop an aggressive phenotype and showed a similar immune infiltration profile to the rejected tumors.

These findings were confirmed using TCGA data of patients with melanoma. Overall patient survival was significantly higher in tumors with low *MIF* expression, especially when considering T cell infiltration. This is consistent with the detrimental influence of high *MIF* levels on the human antitumor immune response (32–35). Future studies should evaluate whether immune checkpoint blockade (ICB) efficacy in highly homogeneous tumors correlates with *MIF* levels. This analysis is currently impossible because of the low number of such patients.

We suggest that increased *Mif* in low-ITH tumors binds to the CD74 receptor (55, 56, 69), potentially recruiting $CD74^+$ macrophages that differentiate into TAMs and exhibit an M2-like signature. These TAMs would reduce tumor infiltration by $CD4^+$ and $CD8^+$ T cells, thus weakening antitumor immunity through a range of effects manifested by dampening of TIL cytotoxicity, effector cytokine secretion, proliferation, and a high T cell exhaustion signature. In contrast, highly homogeneous tumors with reduced *Mif* expression contain fewer proliferating macrophages, potentially increasing tumor infiltration by $CD4^+$ and $CD8^+$ T cells, elevating effector cytokines, and enhancing immune-mediated tumor rejection.

Although high *MIF* expression correlates with robust immunosuppression, increased tumor growth, and poor outcome (32–36, 70), *Mif* has also, paradoxically, been associated with better prognosis. By focusing on highly homogeneous tumors using SCC-derived highly clonal tumors, *Mif* clearly emerged as a consistent and robust biomarker for tumor aggressiveness. Our follow-up single *Mif* KO functional data support our hypothesis, providing a clear-cut phenotype. Importantly, *Mif* and additional targets were likely missed in previous CRISPR screens because (i) CRISPR screens are performed in heterogeneous tumor settings and (ii) CRISPR also targets genes encoding secreted factors. As these secreted factors are provided by neighboring cells, the KO effects will be weaker and masked by other cells that dilute their phenotypic effect. Our findings show the value of evaluating resistance mechanisms in a highly homogeneous system.

Although our experimental system cannot fully recapitulate natural tumor evolution, it has revealed a robust role for high *MIF* expression, potentially important for treating low-ITH and high-*MIF* patients (71). Indeed, MIF inhibitors, including ISO-1, ISO-66, CPSI-1306, and IPG1094, can decrease tumor growth in tumors including melanoma (33, 72–79). Our highly homogeneous model may thus provide an effective platform to evaluate how MIF inhibitors affect tumor growth and immune cell infiltration. In conclusion, we suggest that MIF levels significantly affect the immune response in highly homogeneous melanomas, highlighting this factor as a potential target for future therapies.

METHODS

Mice

Animals were maintained in a specific pathogen–free temperature-controlled (22°C ± 1°C) mouse facility on a reverse 12-hour light, 12-hour dark cycle at the Weizmann Institute of Science. Food and water were given *ad libitum*. Mice were handled using protocols approved by the Weizmann Institute Animal Care Committee (IACUC 05640723-1) in accordance with international guidelines. To generate syngeneic mouse cancer models, 6-week-old female C57BL/6 (purchased from Envigo, RRID: MGI:2159769) and NSG (The Jackson Laboratory, RRID: BCBC_4142) mice were used.

Cell Line B2905

The murine melanoma B2905 cell line (ATCC Cat. #CRL-3476, RRID: CVCL_B0CG) was derived from a UV-irradiated hepatocyte growth factor transgenic mouse in a C57BL/6 background (40) and received under a materials transfer agreement in 2017 from Dr. Glenn Merlino from the NCI, NIH. The cell line was grown in RPMI (Biological Industries) containing 10% heat-inactivated FBS (Gibco), 1% L-glutamine (Biological Industries), 1% penicillin/streptomycin antibiotic (Invitrogen), and 12.5 mmol/L 2-[4-(2-hydroxyethyl)piperazin-1-yl]ethanesulfonic acid (HEPES) buffer (Sigma-Aldrich). All cells were cultured using standard procedures in a humidified incubator at 37°C with 5% CO_2. Cells were tested monthly for *Mycoplasma* using a Mycoplasma EZ-PCR test kit (Biological Industries).

Generation of the Parental UVB-Irradiated Cell Line

Cells of the B2905 mouse melanoma cell line were seeded in 10-cm plates. After 24 hours, at the confluence of 80%, the cells were exposed to a single dose of 600 J/m² UVB radiation using a bench XX-15M 302-nm UV lamp. Irradiation was measured using the UVX radiometer (Ultraviolet Products).

Generation of SCCs

For SCC generation, cells were plated in 96-well plates, at a 1 cell/well concentration. After 10 days of initial plating, cells were monitored, and wells that showed more than one focal clone were excluded. Single clones were passaged to establish cell lines. The number of passages was controlled and documented, and low-passage cells were used for tumor inoculation. Cells were used in the described experiments within a maximum of 2 weeks from thawing.

MHC Flow Cytometry

All SCCs were stained separately for assessment of the expression of MHC-I (BioLegend, Cat. #114607, RRID: AB_313598) and MHC-II (BioLegend, Cat. #116405, RRID: AB_313724) using flow cytometry. Cells were washed twice with PBS, passed through a 70-μm filter (Falcon), and incubated for 30 minutes in magnetic-activated cell sorting (MACS) buffer (Miltenyi Biotec) in the presence of staining

antibodies. Cells were then washed twice, resuspended in MACS buffer, and acquired on a CytoFLEX flow cytometer (Beckman Coulter). For analysis, Kaluza Analysis Software (Beckman Coulter) was used.

In Vitro Proliferation

For *in vitro* proliferation assays, cells were seeded in six replicates (500 cells per well) in 96-well plates and incubated for 7 days. Samples were analyzed every 24 to 48 hours by lysing the cells in 50 mL 0.2% SDS/well and incubating at 37°C for 30 minutes. Following incubation, 150 mL/well of SYBR staining solution [1:750 SYBR Green I (Invitrogen), diluted in water] was added, and the plates were incubated at room temperature in the dark for 10 minutes. Fluorescence intensities were measured for each well using a FLUOstar OPTIMA BMG LABTECH reader.

Tumor Inoculation

For transplantation to C57BL/6 WT mice or NSG immunocompromised mice, 5×10^5 cells in 100 µL PBS were subcutaneously injected into the right lower flank. Tumors were measured using calipers. Tumor volume was calculated using the formula $\pi/6 \times (\text{smallest diameter})^2 \times (\text{largest diameter})$. Tumors were excised for genomic DNA or RNA purification, at days 6, 10, 16, and 20 after inoculation. Tumor-derived SCCs that were rejected within the 33 days of monitoring were designated as "rejected," whereas the others designated as "nonrejected."

Pathologic Analysis to Confirm Tumor Rejection

To confirm the rejection, SCC31 cells were inoculated into immunocompetent mice, and tumor growth was monitored. Following tumor rejection, tissues surrounding the inoculation site were harvested, fixed in 4% (w/v) paraformaldehyde (PFA) for 24 hours, and restored in 1% PFA until embedded in paraffin. Samples were subjected to hematoxylin and eosin staining followed by histologic analysis.

T cell Suppression Assay

Splenocytes were isolated from C57BL/6 mice, enriched for $CD8^+$ and $CD4^+$ T cells using CD4/CD8 (TIL) MicroBeads (Miltenyi Biotec), and labeled with CFSE (5 M, BioLegend). In a 96-well plate precoated with anti–mouse CD3ε (1 µg/mL, SouthernBiotech, Cat. #1535-01, RRID: AB_2794818), 1×10^5 cells in 100 µL per well were plated. Tumors were harvested from mice at day 10 after inoculation and dissociated using gentleMACS and Tumor Dissociation Kit, mouse (Miltenyi Biotec). $F4/8^+$ macrophages were isolated from these tumors using Anti-F4/80 MicroBeads UltraPure (Miltenyi Biotec) and co-cultured with stimulated T cells (1×10^5 cells per well) for 48 hours. The dilution of CFSE was evaluated by flow cytometry.

IFNγ ELISA

To measure IFNγ secretion by T cells co-cultured with the tumor-derived macrophages in the media of the T cell suppression assay, we used Quantikine ELISA Mouse IFNγ Immunoassay (R&D Systems, cat. #MIF00-1) according to the manufacturer's instructions. The supernatant samples were taken after 48 hours and subjected to 1:100 dilution. Each sample was tested in duplicate.

Mif KO Using CRISPR/Cas9

Mif expression was abolished in the nonrejected SCCs using CRISPR–Cas9. Two sgRNAs were designed: "GACGTCAGACTACGT CCCAA" and "AGCCAAGGTGTGCCGGCGGG." Guide RNAs were chosen using the following tools: the MIT CRISPR design tool (80) and sgRNA Designer (81), in their Benchling implementations (www.benchling.com), SSC (82), and CRISPOR (83). Each guide was cloned into a pSpCas9(BB)-2A-GFP vector (RRID: Addgene_48138) and transfected into cells of the nonrejected SCCs. GFP^+ cells were sorted after 2 days, and each cell was seeded in a separate well of a 96-well plate. After 2 weeks of clonal expansion, the KO was confirmed using Sanger sequencing, and SCCs that had WT *Mif* served as controls for the SCCs that had complete KO of the gene, which was later validated using Western blotting as well (Abcam, clone EPR12463, Cat. #ab175189).

In Vivo $CD8^+$ T cell Depletion

To deplete $CD8^+$ T cells, immunocompetent mice were treated with 250 µg of anti-CD8α depleting antibody (Bio X Cell, Cat. #BE0061, RRID: AB_1125541) or IgG2b isotype control (Bio X Cell, Cat. #BE0090, RRID: AB_1107780) intraperitoneal injections, at day −3 (before tumor cell inoculation) and day 0, following flow cytometry validation of definitive depletion of $CD3^+CD8^+$ cells. For flow cytometry validation, blood was obtained from the animal facial vein and stored in ice-cold heparin (Sigma-Aldrich), followed by the removal of blood cells with ACK Lysing Buffer (Gibco). Cells were then stained for FITC anti–mouse CD3 (BioLegend, Cat. #100203, RRID: AB_312660), PE anti–mouse CD4 (BioLegend, Cat. #100511, RRID: AB_312714), and APC anti–mouse CD8 (BioLegend, Cat. #100711, RRID: AB_312750). The mice were further injected with 200 µg of depleting antibody/isotype control routinely at days 3, 7, 10, 14, and 17. At day 20, flow cytometry $CD3^+CD8^+$ depletion validation was performed as described above.

MHC-I Immunopeptidomics

Cell pellets ($n = 3$) were subjected to MHC-I purification as previously described (84, 85). Briefly, cell pellets consisting of 2×10^8 cells were homogenized and lysed with lysis buffer [containing 0.25% sodium deoxycholate, 0.2 mmol/L iodoacetamide, 1 mM EDTA, protease inhibitor cocktail (Sigma-Aldrich), 1 mmol/L phenylmethylsulfonylfluoride, and 1% octyl-β-D-glucopyranoside in PBS] and incubated at 4°C for 1 hour. Lysates were cleared by centrifugation at 4°C, 48,000 *g* for 45 minutes and passed through a preclearing column containing Protein G Sepharose beads (GenScript). MHC-I molecules were immunoaffinity-purified from the cleared lysate using a 1:1 ratio of anti–mouse H-2Db (UNLB, SouthernBiotech, Cat. #1910-01, RRID: AB_2795489) and anti–mouse H-2Kb (Y-3, Bio X Cell, Cat. #BE0172, RRID: AB_10949300) antibodies that were covalently bound to Protein G Resin (GenScript; same beads were used at the preclear step). The MHC–peptide complexes were eluted with 1% trifluoroacetic acid (TFA), followed by purification of the peptides by using a Sep-Pak tC18, 100 mg Sorbent per well, 96-well plate (Waters). Elution of the peptides was done with 28% acetonitrile in 0.1% TFA. In preparation for LC/MS-MS analysis, MHC–peptides were dried by vacuum centrifugation and resolubilized with 0.1% formic acid. For Orbitrap MS-MS experiments, the peptides were separated using reversed-phase chromatography using the nanoACQUITY system (Waters), with a symmetry trap column (180 × 20 mm) and HSS T3 analytic column (0.75 × 250 mm; Waters), with mobile phase A: H_2O + 0.1% formic acid and mobile phase B: acetonitrile + 0.1% formic acid. The peptides were separated with a linear gradient over 2 hours from 5% to 28% B, 28% to 35% in 15 minutes, and 35% to 95% in 15 minutes and maintained at 95% for 10 minutes and back to initial conditions, at a flow rate of 0.35 µL minute^{-1}. The LC was connected online via a nanoelectrospray ionization source (Flexion, Thermo Fisher Scientific) using an emitter (Fossil) to either a Quadrupole-Orbitrap mass spectrometer (Q Exactive HF, Thermo Fisher Scientific) or a Tribrid mass spectrometer (Fusion Lumos, Thermo Fisher Scientific). Data were acquired using a data-dependent method, fragmenting the peptides by higher-energy collisional dissociation. On the Q Exactive HF, full-scan mass spectrometry spectra were acquired at a resolution of 120,000 at 200 m/z with automated gain control (AGC) value of

3×10^6 ions, mass range of 300 to 1,800 Th, and a maximum injection time of 100 ms. MS-MS scans were acquired with an AGC target value of 10^5 with a maximum injection time of 150 ms and isolation of 1.7 Th, and normalized collision energy was set to 30% and MS-MS resolution was 15,000 at 200 m/z. Fragmented m/z values were dynamically excluded from further selection for 20 seconds. On the Fusion Lumos, full-scan MS spectra were acquired at a resolution of 120,000 at 200 m/z with an AGC value of 200%, mass range of 300 to 1,800 Th, and maximum injection time set to auto. MS-MS scans were acquired with an AGC target value of 100% with a maximum injection time of 150 ms and isolation of 1.7 Th; normalized collision energy was set to 27%, and MS-MS resolution was 15,000 at 200 m/z. Fragmented m/z values were dynamically excluded from further selection for 20 seconds. For timsTOF experiments, the peptides were resolubilized with 0.1% TFA and 5 mmol/L tris (2-carboxy-ethyl)-phosphin-HCl before LC/MS-MS analysis. Using nanoElute 2 (Bruker) liquid chromatography, 5 mL of each sample was loaded. Mobile phase A was 0.1% formic acid in water. Mobile phase B was 0.1% formic acid in acetonitrile. Peptides were separated using the Aurora Ultimate C18 nano column, 0.075 × 250 mm (IonOpticks), using a gradient of 2% B to 29% B in 80 minutes, then 0.5 minutes to 95% B, and maintained at 95% B for 2.9 minutes at a flow of 300 nL/minute. The column was placed in the column toaster and connected to a CaptiveSpray electrospray ionization source. The column was maintained at 50°C. Data were acquired with a timsTOF Pro (Bruker) in a data-dependent acquisition, parallel accumulation–serial fragmentation mode with the following parameters: capillary voltage of 1,600 V, temperature of 180°C, mass range of 100 to 1,700 Th, ion mobility of 0.6 to 1.57 1/K0, TIMS ramp time of 300 ms, number of parallel accumulation–serial fragmentation MS-MS scans of 10, target intensity of 20,000 with a threshold of 2,500, charge range of 0 to 5, and a collision energy of 20 at 0.6 1/K0 and 59 at 1.6 1/K0. MS data were analyzed using MaxQuant software (RRID: SCR_014485), with 5% FDR. Peptides were searched against the mouse UniProt data UP000000589. Binding affinity of every mutant peptide was predicted using the NetMHCpan server (RRID: SCR_018182; ref. 86). Subsequently, only neoantigens with a predicted binding affinity of <500 nmol/L were extracted.

Single-cell RNA Library Generation

Tumors were dissociated using Tumor Dissociation Kit and gentleMACS (Miltenyi Biotec) according to the manufacturer's protocol. Single-cell suspensions were hashed using TotalSeq-C anti-mouse Hashtags 1-8 (BioLegend) and stained with propidium iodine (#P3566, Invitrogen). Live cells were then sorted, washed, resuspended in PBS containing 0.04% BSA, and counted using Trypan blue staining. Hashed samples were combined and loaded onto the Chromium Controller (10× Genomics) with a targeted cell recovery of 20,000 cells per library. For the nonrejected versus rejected samples, single-cell gene expression and hash libraries were prepared using the Chromium Single Cell 5′ V(D)J v1.1 Kit with Feature Barcode technology (10× Genomics) according to the manufacturer's protocol. Samples were sequenced on an Illumina NovaSeq using a 150 (read 1) × 8 (index 1) × 150 (read 2) sequencing configuration. For the SCC35 *Mif* KO samples, single-cell gene expression and hash libraries were prepared using the Chromium Single Cell 5′ Reagent Kit v2 (Dual Index) with Feature Barcode technology (10× Genomics) according to the manufacturer's protocol. Samples were sequenced using the Illumina NovaSeq system with a 150 (read 1) × 10 (index 1) × 10 (index 2) × 150 (read 2) sequencing configuration.

sgRNA Pool Design and Cloning

The sgRNA pool was constructed using the previously published protocol for cloning into SCAR vectors [mKate sgRNA backbone (Addgene, #162076, RRID: Addgene_162076), pSCAR_Cas9-blast_GFP (Addgene, #162074, RRID: Addgene_162074), pLX_EFS-Cre_pptdel (Addgene, #162073, RRID: Addgene_162073), and psPAX-D64V (Addgene, #63586, RRID: Addgene_63586); ref. 53].

Briefly, an sgRNA pool was designed with four guides per gene using constructs from the Brie mouse CRISPR Knockout Pooled Library (81). The pool contained 200 nonrejection genes of interest that were significantly upregulated in nonrejected clones compared with rejected clones with an adjusted P value < 0.01 and fold change >1.5 at any time point (219 genes in total; 200 of which were present in the Brie library), 5 nontargeting control guides, as well as 3 depletion controls (*Cd47*, *Adar*, and *Cd274*), and two enrichment controls (*Pten* and *Ccar1*) selected based on previous literature (Supplementary Table S6; Supplementary Table Legends; ref. 52). The oligonucleotides were annealed and then ligated into pSCAR_sgRNA_puro-mKate-lox2272 that had been digested with the enzyme BsmB1. Amplification was performed via electroporation, and guide representation was confirmed by sequencing.

Bulk TCR Sequencing

Genomic DNA was isolated from tumors of mice implanted with rejected, nonrejected, or parental tumor cell lines at day 6, 10, or 15 after implantation. Bulk TCRβ sequencing was performed by Adaptive Biotechnologies (immunoSEQ mmTCRB Service, Deep, RRID: SCR_014709). Processed data were analyzed using R (v4.3.1). We filtered only in-frame TCR rearrangements and calculated Gini indices for each sample using the R package ineq.

Lentivirus Production

Lentivirus was generated as previously described (53). Briefly, integrating lentivirus for both Cas9 and sgRNA was generated by overnight transfection of adherent HEK293 cells (RRID: CVCL_0063) with either the Cas9 or sgRNA vector and the packaging vectors psPAX (Addgene, #12260, RRID: Addgene_12260) and pMD2g (Addgene, #12259, RRID: Addgene_12259). Integrase-deficient lentivirus was generated by transfecting HEK293 cells with the Cre vector, pMD2g, and a variant of the integrase-deficient psPax-D64 (Addgene, #63586, RRID: Addgene_63586). Lipofectamine (Thermo Fisher Scientific) was used as the transfection reagent. The virus was collected at 48 and 72 hours after transfection and then filtered via a 0.45-μm filtration unit (Millipore). The filtered virus was concentrated using the Lenti-X Concentrator (Takara) at 1,500 *g* for 45 minutes. The concentrated supernatant was subsequently aliquoted, flash-frozen, and stored at −80°C until use.

Generation of CRISPR-Edited Cell Lines

Edited SCC lines were generated following the protocol as described by Lane-Reticker and colleagues (54). In brief, plated SCCs were infected with pSCAR_Cas9-blast_GFP lentivirus along with 4 μg/mL of polybrene. The transduction rate was determined by flow analysis of the GFP marker after 48 hours. Once the transduction rate was confirmed to be sufficient, the edited cells were selected with blasticidin for 6 days or until Cas9-expressing cells were >90% of the population. Cas9-expressing cells were then infected with lentivirus for the pSCAR library and underwent selection with puromycin after 48 hours. Cells were selected for 10 days or until edited cells were ≥90% of the population. After 10 days, the cells were infected twice with IDLV-Cre lentivirus in media with polybrene. Using the same process as the other lentivirus infections, cells were monitored for 10 days via flow cytometry for the loss of mKate2 and GFP. After 10 days, >90% of the population was double-negative for fluorescent reporters.

Tumor Inoculation for In Vivo CRISPR Experiments

CRISPR-edited SCC cells were collected and then washed in PBS. A measure of 0.5 million cells in 100 μL of PBS were injected subcutaneously into the left flank of C57BL/6 mice (one tumor per mouse)

and measured every 3 days starting at day 6 after injection. On day 20 after injection, tumors were collected, weighed, and then minced into small pieces. The minced tumors were dissociated using the Miltenyi Tumor Dissociation Kit and a gentleMACS Octo Dissociator with the soft/medium tumor program and then subjected to red blood cell lysis. The resulting cell suspension was then passed through a 70-μm filter and incubated in FACS buffer (PBS supplemented with 1% BSA and 2 mmol/L EDTA) in the presence of Fc block (BioLegend, Cat. #156604, RRID: AB_2783138) and staining antibody (BioLegend, Cat. #103116, RRID: AB_312981). Live CD45 tumor cells were then isolated by FACS before proceeding to library preparation and sequencing.

sgRNA Library Preparation and Sequencing

Genomic DNA was extracted using a commercially available kit (Zymo Research, Cat. #D3025). sgRNA libraries were prepared for sequencing as previously described (87). Briefly, a standard three-step amplification was performed using the P5 and P7 primers listed in Supplementary Table S7 and Supplementary Table Legends. First, sgRNAs were amplified from genomic DNA in 100 μL reactions, with up to 4 μg of gDNA being used per reaction for 22 cycles. For sequencing of plasmid pools, the first PCR was skipped. For the second PCR, 0 to 7 bp offset was added to the library using pooled stagger primers to increase the diversity of the library, with PCR 2 primers targeting sites nested inside of PCR 1 products. Finally, libraries were indexed and then sequenced in dual-indexed 1 × 75 bp format on an Illumina NextSeq sequencer.

WES and RNA-seq Data Processing

Genomic DNA was extracted from cell lines of the SCCs using the QIAGEN DNeasy Blood & Tissue Kit. Exome capture was performed using the SureSelect XT Mouse All Exon Kit (Agilent Technologies). Mapping of WES FASTQ reads to the mouse genome (GRCm38, mm10) was implemented using BWA mem (88). Sorting and indexing of the BAM files were performed using SAMtools v1.8 (RRID: SCR_002105; ref. 89). Subsequently, the Picard MarkDuplicates module was applied. SAMtools mpileup (89) and bcftools v1.3 (RRID: SCR_005227; ref. 89) were used for variant calling. Mouse SNP filtering was applied to the VCF files based on normal mouse spleen and kidney SNPs derived from the injected mouse strain. Furthermore, SNPs obtained from the B2905 parental cell line were removed. RNA was extracted from cell lines and tumors of the rejected and nonrejected SCCs at days 0, 6, 10, 16, and 20 after inoculation, followed by bulk MARS-seq library preparation (90). Sequencing was done using an Illumina NextSeq 500 sequencer using the NextSeq High Output V2 (150 cycles) sequencing kit (Illumina, 150 bp, single reads). RNA-seq bulk sequencing data (from MARS-seq) were analyzed using the User-friendly Transcriptome Analysis Pipeline (UTAP) tool (91).

PCA of Bulk Gene Expression Data

The RNA-seq read count data were trimmed mean of M values (TMM)-normalized and log counts per million (CPM)–transformed with the edgeR package (RRID: SCR_012802; ref. 92) and then subjected to PCA by applying variable standardization. The samples were visualized on a PCA plot showing the top two principal components (PC), and after visual inspection, several outlier samples were identified (including "scc35day16c," "scc31day6c," "scc31day10c," "scc40day10c," "scc32day20a," "scc40day6a," "scc32day6a," "scc37day6c," "scc35day6b," and "scc35day0b") and excluded from the final PCA plot and further analysis. These identified outliers have potential quality issues with higher Ct values and are from the same pool of RNA library preparation.

Analysis of Somatic Mutation Data

VEP (RRID: SCR_007931; ref. 93) was used to annotate the called variants with the reference genome GRCm38 from Ensembl. From the VEP annotation, we extracted information on the gene transcripts mapped to each mutation, as well as the effect of the mutation at the protein level (e.g., amino acid changes, if any). Nonsilent mutations, as described in the main text, were defined as a DNA-level variant with an annotated amino acid change or annotated as a splicing site variant in any of its associated transcripts.

VAF

For each somatic mutation that survived the above-described filtering, the VAF was calculated. This is defined by the number of reads in support of the somatic mutation divided by the total number of reads covering the position of the mutation. The distribution of VAFs was plotted using the probability density function. A threshold of VAF = 0.25 was set to separate clonal from subclonal mutations similar to the definition of Williams and colleagues (41). The term low ITH refers to a VAF value, and a value >0.25 is considered low ITH (homogeneous). Importantly, a low-ITH sample is characterized by a low number of subclonal mutations rather than a low rate of point mutations.

DE and Pathway Enrichment Analysis of Bulk Gene Expression Data

DE analysis comparing the rejected and nonrejected clones was performed with the limma-voom method (94). The DE test was made at each time point, and we also tested for the average DE across all *in vivo* time points (i.e., after transplantation); the tests were conducted using nested design models taking into consideration replicated samples of each clone. We note that we did not use edgeR for testing (although we used edgeR's TMM normalization to obtain a normalized expression matrix as input to several other analyses, e.g., PCA) because it was not able to handle the more flexible nested design model we used for across *in vivo* time points. Gene set enrichment analysis (95), implemented in the fgsea package (RRID: SCR_020938; bioRxiv 2021.02.01.060012), was used for pathway enrichment analysis based on DE log fold-change values, with pathway definitions taken from the Reactome database (96). The Benjamini–Hochberg method was used for multiple hypothesis corrections of *P* values (97). For visualizing the pathway enrichment more intuitively, gene set variation analysis (RRID: SCR_021058; ref. 98) was used to compute per-sample pathway activity score (i.e., the GSVA enrichment score) using the TMM-normalized log CPM expression values, and these scores were used in various plots (but they were not directly used for statistical testing).

Phylogenetic Analysis of Mouse UVB and SCCs

WES data for the UVB-exposed sample (n = 1) and individual SCCs (n = 40) were used for joint clustering to infer the subclones present across this combined set of samples. MAF files containing somatic copy-number alterations (SCNA), generated using CNVkit (RRID: SCR_021917; ref. 99), were used as input to the SciClone algorithm (100). SciClone is a computational method that identifies the number and genetic composition of subclones by analyzing the VAFs of somatic mutations and SCNAs. The method identifies the fraction of cells containing specific mutations and clusters them into subclonal populations. To ensure high confidence, clonal markers were used, and the following variant filters applied: (i) a minimum alternative read depth of >5 was used, (ii) indels and triallelic sites were excluded, and (iii) only variants present in ≥2 samples were retained (i.e., private mutations only in one sample were excluded). This latter criterion of filtering out private variants was implemented to minimize the impact of technical artifacts, which

are known to be a potential issue in ITH analyses (101), as well as the fact that variants found only in one sample offered minimal utility in inferring the overall cross-sample phylogeny. SciClone was run with copyNumberMargins = 0.5, maximumClusters = 30, and minimumDepth = −1 (variants were already prefiltered for a minimum depth of >5 alternative reads during MAF file creation). The clustering solution from SciClone was manually reviewed, and any obvious poor-quality clusters was removed (e.g., clusters defined by <10 mutations; clusters present in every sample but with low VAF values (<25%); and duplicated clusters). The clustered mutations were then inputted to the R package CloneEvol (82) to generate the phylogenetic tree and representative sample tumor diagram. Individual SCCs were mapped to terminal clones/branches (from the overall clustering solution) based on the closest fitting VAF (102).

Rational for SCC Selection and Growth Phenotype Definition

Our aim was to establish a highly controlled model system that uses highly homogeneous SCCs with reproducible growth of both rejection and nonrejection phenotypes that would allow us to compare the two groups and identify the differences contributing to this phenomenon. To better define aggressive versus nonaggressive SCCs, we assessed the growth kinetics of each SCC by calculating the difference in tumor volume between days 6 and 20 after inoculation and comparing it with the UVB-irradiated parental line, which is highly heterogeneous and forms large tumors when injected into immunocompetent mice. Significant differences were found only between UVB and SCC31 or SCC40, which were thus defined as nonaggressive, in comparison with SCC32, SCC35, and SCC37, which had similar growth kinetics as the UVB cell line. These were therefore defined as aggressive. To establish the model system, we searched for a terminal branch that contains more than six SCCs to have a sufficient number of cell clones to examine. Only two terminal branches had more than six SCCs, TB-2 and TB-3. Although TB-3 contained both rejected and nonrejected SCCs (Fig. 1B), the SCCs in TB-2 showed a uniform phenotype of cell growth, which only started at day 25 and, therefore, did not contain both cases of rejected and nonrejected SCCs. In addition, when computing the difference in tumor volume between days 6 and 20 after inoculation for SCCs clustered to TB-2 and calculating the change in tumor growth for each SCC, there was no significant difference between the SCCs, except for two pairs, SCC10 with SCC17 (P value = 0.018) and SCC10 with SCC38 (P value = 0.0038), suggesting that the growth of almost all SCCs in this branch is similar. Indeed, no representation of the two sought growth phenotypes (rejected and nonrejected) was found. Given these results, we decided to focus our studies on the SCCs found in TB-3.

DE of Rejected versus Nonrejected Tumor Clones

To characterize differences between rejected and nonrejected SCCs, DE analysis was performed on tumor cells at each time point (days 0, 6, 10, and 16 after inoculation) separately using the Wilcoxon rank-sum test. Significantly differentially expressed genes were defined as those with a 1.5-fold difference in mean log-normalized expression between the rejected and nonrejected group and a Bonferroni-corrected adjusted P value < 0.01. Core rejection and nonrejection signatures were defined per time point (days 0, 6, and 10 after inoculation) by averaging the expression of significant genes per SCC, scaling the averaged expression values across all SCCs, and identifying genes that displayed a consistent pattern among all rejected or nonrejected SCCs, respectively (i.e., the core nonrejected signature includes genes for which the z-score is >0.1 in all nonrejected SCCs and is <0 for all rejected SCCs). The core signature analysis was not performed for the day 16 time point because there was only one rejected clone (SCC40) present.

Estimating Cytolytic Activity from RNA-seq Data

The gene expression levels in the units of reads per kilobase of transcript per million mapped reads (RPKM) of the 330 patients with melanoma with corresponding survival information were downloaded from TCGA portal (103). The cytolytic activity of TILs in patient tumors was estimated from the geometric mean of the expression levels of GZMA and PRF1.

$$CYT = \exp\left(\frac{\ln(GZMA+1)+\ln(PRF1+1)}{2}\right)$$

wherein CYT is the cytolytic activity.

Computation and Analysis of T cell Function and T cell Infiltration Scores Using Bulk Gene Expression Data

The TIDE (43) algorithm was applied to the bulk RNA-seq data to compute measures of T cell function from gene expression. We used the offline TIDEpy package with default normalization and parameters. TIDE was initially used to predict ICB therapy response via computing two different scores for each sample: a T cell "dysfunction" score and a T cell "exclusion" score. In principle, these scores can be used to reflect antitumor immune function, and we used TIDE for this alternative purpose. The cell infiltration score that we describe in this study is the negative of the "exclusion" score from TIDE. The "dysfunction" score from TIDE is higher in ICB responders and thus seems to be a misnomer because this score positively correlates with T cell function. Therefore, we call it the T cell function score in this study. The differences in these scores between the rejected and nonrejected clones were tested with a linear model at each time point; the tests were conducted using nested design models, taking into consideration the replicated samples of each clone. The Benjamini–Hochberg method was used for multiple hypothesis corrections of P values.

T cell Exhaustion Score Analysis

A T cell exhaustion signature (a plastic dysfunctional state from which T cells can be rescued) of 25 genes from Philip and colleagues (104) was used to score the exhaustion of individual $CD8^+$ T cells in each clone.

Data Processing of Hashed scRNA-seq Libraries

Reads from single-cell RNA expression libraries were aligned to mouse genome assembly GRCm38 (mm10) and quantified using the Cell Ranger count (10× Genomics, version 6.0.0). The filtered feature-barcode matrices containing only cellular barcodes were used for further analysis. Single-cell gene expression matrices were imported into R (version 4.2.0) and analyzed using Seurat (version 4.3.0; RRID: SCR_016341; ref. 105). Cells with a number of genes captured between ±2 SDE per library were kept. Additionally, cells with >10% mitochondrial RNA reads were excluded from subsequent analyses. Libraries were demultiplexed using HTODemux() with a positive quantile of 0.99. Only cells that were identified as a singlet were kept for downstream processing. For each library, log normalization and variable feature selection based on variance-stabilizing transformation were first performed on each sample individually. Then anchors between samples were identified using FindIntegrationAnchors() and integrated using IntegrateData() with 30 dimensions. The integrated expression matrix was then scaled and centered for each feature. Next, linear dimensional reduction was performed on the integrated scaled data using PCA. For visualization, uniform manifold approximation and projections were calculated using the first 30 PCs. To identify clusters based on gene expression profiles, we performed shared nearest neighbor modularity optimization clustering.

Calculation of M2 Macrophage Score

Cell-cluster/type compositions are plotted using the dittoBarPlot() function from the dittoSeq package (106). The annotation of M1 and M2 macrophages is based on the Tumor Immune Single-cell

Hub (59) annotation for the BRCA_GSE114727_inDrop dataset published by Azizi and colleagues (107). The top 100 marker genes for each cell type were downloaded from the Tumor Immune Single-Cell Hub and used to calculate the M1 and M2 scores for each cell using the Seurat AddModuleScore() function. Violin plots of gene signature scores were calculated using the Seurat VlnPlot() function.

Gene Expression Pattern Analysis

Expression patterns of the C1q subunit and *Apoe* genes are plotted using the Seurat FeaturePlot() function.

Tumor CNV Prediction

Tumor cells were distinguished from nonmalignant stromal cells by predicting CNVs using the infercnv R package (v1.18.1; RRID: SCR_021140). scRNA-seq raw count matrices were used as input, with a minimum average count cutoff of 0.1 per gene. Single cells were grouped by cell-type cluster annotations, using all cells from immune clusters as a reference group. CNV prediction was then run using the six-state i6 hidden Markov model.

Hierarchical Clustering of Tumor Clones

To assess the transcriptional similarity between rejected, non-rejected, *Mif* KO, and control tumor cells, scRNA-seq data were subsetted to cells belonging to tumor clusters. Pseudobulk transcriptional profiles were generated for each condition replicate by averaging normalized expression values. PCs were computed using the top 2,000 most variable genes across all samples. We observed that the first two PCs corresponded to scRNA-seq experimental batch and time point, respectively. To avoid these technical factors influencing the clustering, we omitted these first two components and performed hierarchical clustering on PCs 3 to 30 for each time point separately using Euclidean distance and Ward D2 agglomerative clustering.

Differentially Expressed Gene and Pathway Analysis

DE analysis of *Mif* KO and control tumor cells was performed at each time point using the Wilcoxon rank-sum test with Bonferroni correction. Significantly enriched Molecular Signatures Database hallmark gene sets in each condition were defined with a Benjamini–Hochberg adjusted q-value < 0.05 and computed using the clusterProfiler package (v3.14.3; RRID: SCR_016884; ref. 108).

Opal Multiplex IHC Staining of Mouse Samples

For Opal Multiplex IHC staining, tumors were excised at day 10 after inoculation, fixed in 4% (w/v) PFA for 24 hours, and restored in 1% PFA until embedded in paraffin for histologic analysis. IHC was performed on deparaffinized and rehydrated 4-μm-thick paraffin-embedded sections using xylene and a decreasing concentration of ethanol (100%, 96%, and 70%). Endogenous peroxidase activity was blocked with 3% H_2O_2 and 1% HCl in methanol for 30 minutes, followed by heat-induced antigen retrieval in Tris-EDTA (pH = 9). For nonspecific binding, sections were blocked with 20% normal horse serum (NHS, VectorLabs, S-2000) and 0.1% Triton. In case a secondary biotinylated antibody was used, an additional step of biotin blocking kit (VectorLabs, SP-2001) was performed. Primary antibodies, diluted in 2% NHS and 0.1% Triton, were incubated overnight (Supplementary Table S8; Supplementary Table Legends). The samples were stained with F4/80 (Cell Signaling Technology, Cat. #70076, RRID: AB_2799771), CD206 (Abcam, Cat. #ab64693, RRID: AB_1523910), and CD204 (Cell Signaling Technology, Cat. #98215, RRID: AB_3665150). Incubation with secondary horseradish peroxidase antibodies (Jackson ImmunoResearch Labs, Cat. #711-035-152, RRID: AB_10015282) was followed by fluorescently labeled Opal reagents. Antibodies were removed by 10 minutes of microwave treatment with Tris-EDTA (pH = 9), and then the protocol repeated from the blocking step.

CODEX Multiplexed Tissue Imaging

For CODEX multiplexed imaging, tumors were excised at day 6 after inoculation, fixed in 4% (w/v) PFA for 24 hours, and restored in 1% PFA until being embedded in paraffin for histologic analysis. The tissue was pretreated by heating the slides in an incubator for 70°C for 1 hour to melt the paraffin and improve tissue attachment to the slide. IHC was performed on deparaffinized and rehydrated 4-μm-thick paraffin-embedded sections using xylene and a decreasing concentration of ethanol (100%, 95%, 80%, and 70%). For antigen retrieval, the slides were heated in antigen retrieval buffer (pH = 9) in a PT Module, followed by washing steps with ddH_2O and tris-buffered saline with tween 20 (TBST) and blocking with CODEX formalin-fixed, paraffin-embedded (FFPE) blocking solution for 1 hour at room temperature in a humidity chamber. The tissue was incubated overnight at 4°C with the antibody mix diluted in FFPE blocking solution (Supplementary Table S9; Supplementary Table Legends). The samples were stained with CD3 (Abcam, Cat. #Ab251607, RRID: AB_3662950), CD8 (Cell Signaling Technology, Cat. #60168, RRID: AB_2756376), TIM3 (Abcam, Cat. #Ab242080, RRID: AB_2888936), LAG3 (Abcam, Cat. #Ab251606, RRID: AB_3094609), CD45 (Cell Signaling Technology, Cat. #98819, RRID: AB_2799780), and Ki67 (BD Biosciences, Cat. #556003, RRID: AB_396287). Oligoconjugated primary antibodies were prepared 50 μg at a time, precisely as detailed by Black and colleagues (109). The next day, the tissue was fixated with three fixation steps. First, the antibodies were fixed with PFA fixation solution, followed by treatment with ice-cold methanol for the precipitation of proteins, removement of lipids from cells and clearing fluorescent reporters with the cell membranes, and finally the incubation with the final fixative solution (BS3 in PBS) for maintaining CODEX antibodies bound to the tissue for the hybridization and stripping cycles during imaging. Until the run of the experiment, the specimens were stored in CODEX staining buffer (S4) solution at 4°C. Using the Experiment Designer, all PhenoCycler Reporters were assigned to a cycle number, and the cycles were associated with specific wells. For each cycle, a reporter master mix was prepared by diluting each reporter in a buffer plate, and for each run, two blank cycles with the buffer plate were prepared. During the PhenoCycler run, in each cycle, the instrument withdrew the reporter master mix from one well of the 96-well plate. After antibody labeling, a flow cell was affixed to the tissue slide. Then the slide was mounted into the stage carrier and placed into the PhenoCycler-Fusion PhenoImager (Akoya Biosciences), and multicycle imaging was initiated using 20× magnification.

Multiplex Fluorescence Imaging

Multispectral imaging was performed using PhenoImager at 20× magnification (Akoya Biosciences, RRID: SCR_023772) according to the manufacturer's instructions. Later, the multispectral acquired images were loaded into inForm software for unmixing and background subtraction (inForm v.3.0; Akoya Biosciences, RRID: SCR_019155). In inForm software, an unstained slide [without 4′,6-diamidino-2-phenylindole (DAPI) and Opal staining] was loaded, and regions with high autofluorescence signals were marked for processing. After processing, image tiles were stitched using QuPath software (RRID: SCR_018257) with the "merge multiple TIFF fields" script.

Image Processing

To detect and quantify the macrophages ($F4/80^+$, $CD204^+$, and $CD206^+$) and T cells ($CD3^+$ and $CD8^+$), cell segmentation and classification were applied to the fluorescent marker–stained images using

QuPath (v0.4.3; ref. 110). The nuclei were segmented from the DAPI channel using StarDist (111) and further inflated to have approximated cell segmentation. The cells were then classified as positive or negative for each of the stains, and the total number of double- or triple-positive cells and their respective ratios were quantified within five representative regions of 500 × 500 μm for each tumor. To improve nuclei segmentation, a new StarDist model was trained using the ZeroCostDL4Mic (112) StarDist notebook with examples that were not perfectly segmented by the provided model. Positive/negative Random Trees cell classifiers were trained for each stain independently on multiple image regions representative of the tissue characteristics and experimental conditions. The classifiers were then combined together to detect double- and triple-positive cells. The classifiers were then applied to selected representative areas of the tumors based on a threshold classifier to quantify the total number of double- ($CD3^+$ and $CD8^+$ T cells) and triple-positive ($F4/80^+$, $CD204^+$, and $CD206^+$ macrophages) cells and their respective ratios to the total number of cells per tissue regions of interest.

CyTOF Sample Preparation and Data Acquisition

Antibodies were obtained preconjugated to heavy-metal isotopes from Fluidigm or IONpath, or conjugated via the MIBItag Conjugation Kits (IONpath). The samples were stained with TIM3 (Standard BioTools, Cat. #3162029, RRID: AB_2687841), CD8 (Standard BioTools, Cat. #3153012B, RRID: AB_2885019), Cx3cr1 (Standard BioTools, Cat. #92J020155, RRID: AB_3665151), CD62L (Standard BioTools, Cat. #3160008, RRID: AB_2687840), TCRβ (Fluidigm, Cat. #3143010B, RRID: AB_3665159), CD3 (Standard BioTools, Cat. #3152004, RRID: AB_2687836), CTLA-4 (Fluidigm, Cat. #3154008B, RRID: AB_3665152), PD-1 (Standard BioTools, Cat. #3159024, RRID: AB_2687839), CD44 (Standard BioTools, Cat. #3171003B, RRID: AB_2895121), GrnzB (Standard BioTools, Cat #3173006B, RRID: AB_2811095), Lag3 (Standard BioTools, Cat. #3174019B, RRID: AB_3665154), ICOS (Fluidigm, Cat. #3176014B, RRID: AB_3665155), CD4 (Standard BioTools, Cat. #3145002B, RRID: AB_2687832), CCR7 (Standard BioTools, Cat. #92J015163, RRID: AB_3665153), CD25 (Standard BioTools, Cat. #3151007B, RRID: AB_2827880), Foxp3 (Standard BioTools, Cat. #3165024, RRID: AB_2687843), MHC-II (Standard BioTools, Cat. #3209006B, RRID: AB_2885025), iNOS (Standard BioTools, Cat. #3161011B, RRID: AB_2922920), CD80 (Fluidigm, Cat. #92J023158, RRID: AB_3665158), F480 (Standard BioTools, Cat. #3146008B, RRID: AB_2895117), CD11b (Standard BioTools, Cat. #3148003B, RRID: AB_2814738), Ly6C (Standard BioTools, Cat. #3150010B, RRID: AB_2895118), CD206 (Standard BioTools, Cat. #3169021B, RRID: AB_2832249), CD86 (Standard BioTools, Cat. #3172016B, RRID: AB_2922923), and Ki67 (Standard BioTools, Cat. #3168007B, RRID: AB_2800467). Targets were allocated to specific heavy-metal isotopes following the sensitivity of the mass cytometer (e.g., placing lower abundance targets on higher sensitivity channels) and to avoid potential spillover. Briefly, the tumors were harvested and dissociated using collagenase IV and DNaseI for 40 minutes at 37°C and gentleMACS (Miltenyi Biotec). All individual samples were incubated with mouse TruStain FcX (anti–mouse CD16/32, BioLegend, Cat. #101301, RRID: AB_312800) for 15 minutes on ice. To eliminate technical variability during staining or acquisition, individual samples within one experiment were barcoded with a unique combination of cadmium-tagged CD45 antibodies (Fluidigm; ref. 113) for 30 minutes on ice, washed, and combined into a composite sample. Cell surface antibody master mix was added to the composite sample. After incubation for 30 minutes on ice, cells were washed once prior to being labeled with Cell-ID Cisplatin viability stain according to the manufacturer's instructions. To enable intracellular staining, True-Nuclear Transcription Factor Buffer Set (BioLegend) was used according to the manufacturer's instructions. Cells were fixed for 1 hour at room temperature, washed with permeabilization buffer, and intracellular antibody master mix that was diluted in permeabilization buffer was added to the composite sample and incubated for 30 minutes at room temperature. Cells were washed with permeabilization buffer and then Maxpar Cell Staining Buffer. After washing, composite samples were incubated overnight in 4% formaldehyde (Thermo Fisher Scientific) in Maxpar PBS at 4°C. The following day and prior to acquisition, the samples were incubated with Cell-ID Intercalator-Ir for 30 minutes, washed twice with Maxpar Cell Staining Buffer, and resuspended in Maxpar PBS. The samples were then processed via the MARS Sample Preparation system (Applied Cells), to enrich for single cells, according to the manufacturer's instructions, and then washed twice with Maxpar Cell Acquisition Solution Plus. The composite sample was then resuspended in Cell Acquisition Solution Plus containing 1:10 EQ Four Element Calibration Beads (Fluidigm), filtered through a cell strainer (BD) of 35 μm pore size, and acquired on a Helios CyTOF system (Fluidigm).

CyTOF Data Preprocessing

Raw CyTOF data were first bead-normalized to remove acquisition sensitivity–related influences on marker expression by using Fluidigm's software (RRID: SCR_021055). Normalized data were uploaded to the FlowJo analysis platform (RRID: SCR_008520) to identify single, live cells by excluding the remaining beads (^{140}Ce and ^{153}Eu) and gating on DNA (^{193}Ir) and viability (^{195}Pt) channels. Next, barcoded cells were assigned back to their initial samples using their unique cadmium barcode combination with the MATLAB single-cell debarcoder (113). Data were subsequently imported into FlowJo software (BD) for downstream analysis.

CyTOF Data Analysis

Immune populations were manually gated (CD8 T cells: $CD3^+$ $TCR\beta^+CD8^+CD4^-$; CD4 T cells: $CD3^+TCR\beta^+CD4^+CD8^-$; and macrophages: $CD11b^+F480^+$), and then Leiden community detection was performed using CellEngine (CellCarta, RRID: SCR_022484) software. Leiden clustering parameters were 90 neighbors and 0.15 resolution. CD8 T cells were clustered using the markers TIM3, CCR7, CD25, CD8, Cx3cr1, CD62L, TCRβ, CD3, CTLA4, PD-1, CD44, GrnzB, Lag3, and ICOS. CD4 T cells were clustered using the markers TIM3, CCR7, CD25, Cx3cr1, CD62L, Foxp3, TCRβ, CD4, CD3, CTLA-4, PD-1, CD44, GrnzB, Lag3, and ICOS. Macrophages were clustered using the parameters MHCII, iNOS, Cx3cr1, CD80, F480, CD11b, Ly6C, CD206, and CD86.

Opal Multiplex IHC Staining of Human Samples

TMAs 256, 257, and 258 were created using 1mm punches from FFPE blocks of patients diagnosed with stage III and IV metastatic melanoma, who were treated at the University Hospital of Zürich following ethics approval KEK-ZH-Nr 2014-0425. The TMAs include samples of immune-inflamed, immune-excluded, and immune-deserted tumors. T cell infiltration was assessed using CD3 staining in whole-tumor slides. For tumors with multiple biopsies, samples were taken from both the tumor core and margin. Specifically, we stained for MIF (Atlas Antibodies, Cat. #HPA003868, RRID: AB_1079290), T cells [CD3 (Agilent, Cat. #IS50330-2, RRID: AB_2732001)], M2 macrophages [CD163 (Leica Biosystems, Cat. #CD163-L-CE, RRID: AB_2920861) and CD68 (Cell Signaling Technology, Cat. #76437, RRID: AB_2799882)], and tumor cells [S100 (Leica Biosystems, Cat. #NCL-L-S100p, RRID: AB_564003) and MelanA (Novus, Cat. #NBP1-30151, RRID: AB_1987285); Supplementary Table S10; Supplementary Table Legends]. The staining protocol was run on the Leica Biosystems BOND RX, followed by multispectral imaging with the Vectra Polaris (RRID: SCR_025508). Image processing and analysis

were conducted using QuPath software v0.4.3 (RRID: SCR_018257). The TMA tissue cores were selected using the TMA dearrayer, and the nuclei were segmented from the DAPI channel using StarDist and further inflated to have approximated cell segmentation. To improve nuclei segmentation, a new StarDist model was trained using the ZeroCostDL4Mic StarDist notebook with examples that were not perfectly segmented by the provided model. The cells were then classified as positive or negative for each of the stains, and the total number of single or double cells and their respective ratios were quantified within each tumor. Positive/negative Random Trees cell classifiers were trained for each stain independently on multiple image regions that were representative of the tissue characteristics and experimental conditions. The classifiers were then combined to detect double-positive cells. The classifiers were then applied to each TMA to quantify the total number of MIF$^+$ cells, CD3$^+$ T cells, double-positive CD68$^+$ CD163$^+$ M2 macrophages, and double-positive S100$^+$ MelanA$^+$ tumor cells and their respective ratios to the total number of cells per TMA tissue core.

Statistical Analysis of TMA of Biopsies from Patients with Cancer

TMAs 256, 257, and 258 were used for the analysis. For each biopsy, the number of positive detections were divided by the total number of detections (for CD3, MIF, and CD68/CD163 individually). The percentages obtained were categorized into three groups based on the level of T cell infiltration. Samples lacking information on T cell infiltration were discarded. For CD3-positive plot, 242 biopsies from 126 patients were analyzed. In the MIF-positive plot, 243 biopsies from 129 patients were analyzed. The distribution of values for the biopsies was plotted using R version 4.1.0. Statistical significance was not calculated because information on cancer heterogeneity of the samples was not available to be included in the statistical model. The correlation between %MIF-positive and %CD68 and CD163 double-positives was calculated using the Pearson correlation and significance calculated. This analysis includes 248 samples associated with 129 patients.

CRISPR Pooled Screen Data Analysis

sgRNA libraries from the pooled CRISPR screens were analyzed using the MAGeCK pipeline (RRID: SCR_025016; ref. 114). Briefly, sgRNA counts are first computed per library using the MAGeCK count and median normalized in order to adjust for library sizes and read count distributions. Then sgRNA libraries sequenced on day 20 after tumor inoculation were compared with the input guide library using the MAGeCK test to identify enriched and depleted guides and genes.

Cell–Cell Communication and Signaling Pathway Analysis

To infer cross-talk between tumor and immune cell types, cell–cell communication analysis was performed with CellPhoneDB v2.0.0 (RRID: SCR_017054). First, the rejected versus nonrejected scRNA-seq data were downsampled to 500 cells per cell-type cluster. Normalized scRNA-seq counts and cell-type cluster identities per cell were used as the input to the statistical method of CellPhoneDB for 1,000 iterations. Interaction pairs with statistical significance at a P value threshold 0.05 were then ranked by interaction scores (means).

To identify differential cell-type communication between rejected and nonrejected tumors, the signaling pathway analysis was performed with CellChat v2.1.2 (RRID: SCR_021946). Using the mouse CellChat database of "cell–cell contact" and "secreted signaling" ligand–receptor interactions, cell–cell communication networks were inferred for rejected and nonrejected clones at each time point (days 6, 10, and 16) separately. For each SCC phenotype and time point, overexpressed ligand–receptor interactions in each cell-type group were computed using default parameters. Communication probabilities between cell types were then computed via a permutation test using the "trimean" robust mean method (which approximates 25% truncated mean). Interactions were then aggregated to the level of signaling pathways. To identify the cell types that were involved in each signaling pathway, dominant sender or receiver populations were identified by computing the degree of outgoing and incoming signaling interactions within each cell type. Differential signaling strength between nonrejected and rejected tumors was then computed by taking the difference in total interaction weights for each cell type–cell type communication pair.

Quantification and Statistical Analysis

Statistical analysis not described elsewhere was performed using GraphPad Prism 10 software (GraphPad, RRID: SCR_002798) and the software environment R, using RStudio (RRID: SCR_000432). All data are presented using SEM. P values are depicted in all figures, and selected P values with exceptional significance to the article are also briefly described in the main text. Samples sizes (n), means, and SEM are depicted in the figures and/or figure legends. Sample size values were either depictions of the number of mice used for experiments or the number of patients.

TCGA Survival Analysis

ITH for individual TCGA samples was previously computed using CHAT (115) incorporating somatic variant call data and SCNAs. The ITH calculation using CHAT on input TCGA data was described previously by Wolf and colleagues (5). From the TCGA data access portal, we downloaded level 2 SNP array and germline + somatic variant call data (*.byallele.copynumber.data.txt, *.oxoG.snp.capture.tcga.*vcf*.) for 432 skin cutaneous melanoma tumor and matched normal samples. Across all 432 patients, we applied CHAT with default settings to estimate tumor purity followed by estimation of cellular abundance of CNVs and somatic mutations from the SNP array and variant call data, respectively.

Given that tumor evolution is characterized by a series of clonal expansion events, we often find that mutations and CNVs detected from a bulk tumor sample group into clusters that are laid out on the tumor's evolutionary tree. The number of these clusters or clones is interpreted as the ITH. Using CHAT, we derived two estimates of the number of clones by clustering cellular abundances of somatic mutations (ITH1) or clustering cellular abundances of CNVs (ITH2). Both estimates convey important information of the underlying clonal structure at different resolutions. Hence, we set the overall ITH of a sample as

$$\mathrm{ITH} = \max(\mathrm{ITH1}, \mathrm{ITH2})$$

Given the limitation of a single bulk tumor sample per patient for inference, the above estimate is lower bound and correlated with tumor purity (Spearman $\rho = 0.232$, P value = 2.09E−5).

To test for an association between *MIF* expression and overall patient survival in TCGA, we used previously deconvolved data by cell type (57); deconvolution means that we computationally partitioned the expression of many genes, including *MIF*, in each sample by cell type after estimating the proportions of different cell types in each sample. The deconvolution of TCGA data was done prior to this study and made available in conjunction with Wang and colleagues (57), so we do not specify the methods here. In doing the survival analysis, we used the estimated *MIF* expression in tumor cells as the independent variable and the overall survival time as the (outcome) dependent variable. We further checked for the combination of TIL patterns (58) within high/low *MIF* expression for 377 patients with melanoma in TCGA and observed the effect on overall patient survival. According to Saltz and colleagues (58), pathologists annotated tumors as

"hot" with TILs scattered throughout at least 30% of the tumor's area or immune responses formed band-like boundaries that border the tumor at its periphery. Tumors were annotated as "cold" when loosely scattered TILs were present in <30% but >1% area of the tumor. To assess the immune cell infiltration extent within these annotated cold tumors in patients with melanoma in TCGA, we compared the enrichment of the immune cell infiltration signature of four genes (*GCH1*, *GZMA*, *RARRES3*, and *PSMB8*), as published by Zhu and colleagues (116), in tumors annotated as hot and in those annotated as cold. We fit Kaplan–Meier survival curves for each group to test for any significant survival differences between the groups using the log-rank test. R packages "survival" and "survminer" were used to perform all the survival analyses (117).

To assess whether the identified core rejection and nonrejection gene sets from days 0, 6, and 10 can be used to stratify patients with high/low ITH and patients with tumors of hot/cold annotations, we used 76 human orthologous genes, identified from among 78 mouse genes for the union of the gene sets from the three time points. We specifically identified 4, 10, and 12 human genes for days 0, 6, and 10, respectively, from the corresponding mouse core rejection gene sets and 26, 13, and 11 human genes for days 0, 6, and 10, respectively, from the corresponding mouse core nonrejection gene sets.

Data Availability

All scRNA-seq datasets generated in this study have been deposited in NCBI Gene Expression Omnibus and are publicly accessible under accession number GSE247059. CyTOF data are available via Mendeley Data (https://data.mendeley.com/datasets/hkhvksr37m/1).

Authors' Disclosures

K. Cheng reports current employment with MSD R&D Co. Ltd. This study is not related to his current work at MSD. M.P. Levesque reports grants from Roche, grants and personal fees from Oncobit, Scailyte, and Bacoba, and personal fees from Danaher outside the submitted work. A.T. Satpathy reports personal fees from Immunai, Cartography Biosciences, Santa Ana Bio, Prox Biosciences, and 10x Genomics and grants from Astellas and Merck Research Laboratories outside the submitted work. Y. Samuels reports personal fees and grants from Achilles Therapeutics UK Ltd outside the submitted work. No disclosures were reported by the other authors.

Authors' Contributions

S. Cohen Shvefel: Conceptualization, validation, investigation, visualization, writing–original draft, writing–review and editing. **J.A. Pai:** Conceptualization, investigation, visualization, writing–original draft, writing-review and editing. **Y. Cao:** Formal analysis. **L.R. Pal:** Formal analysis. **O. Bartok:** Validation, investigation. **R. Levy:** Formal analysis. **M.J. Zemanek:** Validation, visualization. **C. Weller:** Validation. **E. Herzog:** Investigation. **W. Yao:** Validation. **K.J. Hiam-Galvez:** Formal analysis. **K. Cheng:** Formal analysis. **Y. Yin:** Validation. **P.P. Du:** Validation. **C.J. Raposo:** Validation. **N. Gumpert:** Investigation. **M. Welti:** Resources. **J.M. Martínez Gómez:** Resources. **F. Sella:** Resources. **E. Yakubovich:** Validation. **I. Orr:** Investigation. **S. Ben-Dor:** Investigation. **R. Oren:** Investigation. **L. Fellus-Alyagor:** Investigation. **O. Golani:** Formal analysis. **O.J. Brenner:** Investigation. **T.M. Salame:** Investigation. **M. Zerbib:** Investigation. **I. Goliand:** Visualization. **D. Ranmar:** Visualization. **I. Savchenko:** Visualization. **N. Ketrarou:** Visualization. **A.A. Schäffer:** Formal analysis. **R. Dahan:** Supervision. **M.P. Levesque:** Supervision. **E. Ruppin:** Supervision, writing–original draft, writing–review and editing. **A.T. Satpathy:** Conceptualization, supervision, writing–original draft, writing–review and editing. **Y. Samuels:** Conceptualization, supervision, writing–original draft, writing–review and editing.

Disclaimer

Views and opinions expressed in this article are those of the authors alone and do not necessarily reflect those of the European Union or the European Research Council. Neither the European Union nor the granting authority can be held responsible for them.

Acknowledgments

Y. Samuels is supported by the Israel Science Foundation grant number 2133/23, the European Research Council (ERC) under the European Union's Horizon 2020 Research and Innovation Programme (grant agreement number 770854), and the European Union (European Research Council, Mel-Immune, 101094980). This research was further supported by the Center for Immunotherapy at the Weizmann Institute of Science, the MRA (917324), the Minerva Stiftung with the funds from the BMBF of the Federal Republic of Germany , the ICRF (20-802-ICG), the Alisa and Peter Savitz Foundation, Les and Cyndy Lederer, Brenda Gruss and Daniel Hirsch, the Donald Gordon Foundation, the Sigmund and Sofie Englander Foundation, Ted and Sylvia Quint 78775, Margaret and Leo Meyer and Hans M. Hirsch Foundation 77888, Estate of Rena G. Moses 111677, Samowitz Foundation Trust 74163, the Dwek Institute for Cancer Therapy Research, the Estate of Gerald Alexander, the Estate of Jackson Toby, and the Estate of Gertrude Buchler, as well as Laboratory in the name of M.E.H Fund established by Margot and Ernst Hamburger. This research was supported in part by the Intramural Research Program of the NIH, NCI. Y. Samuels is the incumbent of the Knell Family Professorial Chair. Y. Samuels is the Director of the Moross Integrated Cancer Center. A.T. Satpathy was supported by a Career Award for Medical Scientists from the Burroughs Wellcome Fund, a Lloyd J. Old STAR Award from the Cancer Research Institute, a Pew-Stewart Scholars for Cancer Research Award, and the Parker Institute for Cancer Immunotherapy. The images in this article were acquired at the Advanced Optical Imaging Unit, de Picciotto-Lesser Cell Observatory unit at the Moross Integrated Cancer Center, Life Science Core Facilities, Weizmann Institute of Science. This work used the computational resources of the NIH HPC Biowulf Cluster (http://hpc.nih.gov). J.A. Pai was supported by NIH Training Grant 5T32AI007290.

Note

Supplementary data for this article are available at Cancer Discovery Online (http://cancerdiscovery.aacrjournals.org/).

Received November 29, 2023; revised September 11, 2024; accepted November 18, 2024; published first November 20, 2024.

REFERENCES

1. Andor N, Graham TA, Jansen M, Xia LC, Aktipis CA, Petritsch C, et al. Pan-cancer analysis of the extent and consequences of intratumor heterogeneity. Nat Med 2016;22:105–13.
2. Morris LGT, Riaz N, Desrichard A, Şenbabaoğlu Y, Hakimi AA, Makarov V, et al. Pan-cancer analysis of intratumor heterogeneity as a prognostic determinant of survival. Oncotarget 2016;7:10051–63.
3. McDonald K-A, Kawaguchi T, Qi Q, Peng X, Asaoka M, Young J, et al. Tumor heterogeneity correlates with less immune response and worse survival in breast cancer patients. Ann Surg Oncol 2019;26:2191–9.
4. McGranahan N, Furness AJS, Rosenthal R, Ramskov S, Lyngaa R, Saini SK, et al. Clonal neoantigens elicit T cell immunoreactivity and sensitivity to immune checkpoint blockade. Science 2016;351:1463–9.
5. Wolf Y, Bartok O, Patkar S, Eli GB, Cohen S, Litchfield K, et al. UVB-induced tumor heterogeneity diminishes immune response in melanoma. Cell 2019;179:219–35.e21.

6. Gejman RS, Chang AY, Jones HF, DiKun K, Hakimi AA, Schietinger A, et al. Rejection of immunogenic tumor clones is limited by clonal fraction. Elife 2018;7:e41090.
7. Frankell AM, Dietzen M, Al Bakir M, Lim EL, Karasaki T, Ward S, et al. The evolution of lung cancer and impact of subclonal selection in TRACERx. Nature 2023;616:525–33.
8. Dentro SC, Leshchiner I, Haase K, Tarabichi M, Wintersinger J, Deshwar AG, et al. Characterizing genetic intra-tumor heterogeneity across 2,658 human cancer genomes. Cell 2021;184:2239–54.e39.
9. Jamal-Hanjani M, Wilson GA, McGranahan N, Birkbak NJ, Watkins TBK, Veeriah S, et al. Tracking the evolution of non-small-cell lung cancer. N Engl J Med 2017;376:2109–21.
10. Westcott PMK, Muyas F, Hauck H, Smith OC, Sacks NJ, Ely ZA, et al. Mismatch repair deficiency is not sufficient to elicit tumor immunogenicity. Nat Genet 2023;55:1686–95.
11. López-Janeiro Á, Padilla-Ansala C, de Andrea CE, Hardisson D, Melero I. Prognostic value of macrophage polarization markers in epithelial neoplasms and melanoma. A systematic review and meta-analysis. Mod Pathol 2020;33:1458–65.
12. Huang L, Chen H, Xu Y, Chen J, Liu Z, Xu Q. Correlation of tumor-infiltrating immune cells of melanoma with overall survival by immunogenomic analysis. Cancer Med 2020;9:8444–56.
13. Li K, Wang R, Liu G-W, Peng Z-Y, Wang J-C, Xiao G-D, et al. Refining the optimal CAF cluster marker for predicting TME-dependent survival expectancy and treatment benefits in NSCLC patients. Sci Rep 2024;14:16766.
14. Bilotta MT, Antignani A, Fitzgerald DJ. Managing the TME to improve the efficacy of cancer therapy. Front Immunol 2022;13:954992.
15. Ostman A, Augsten M. Cancer-associated fibroblasts and tumor growth-bystanders turning into key players. Curr Opin Genet Dev 2009;19:67–73.
16. Gunaydin G. CAFs interacting with TAMs in tumor microenvironment to enhance tumorigenesis and immune evasion. Front Oncol 2021;11:668349.
17. Nasrollahzadeh E, Razi S, Keshavarz-Fathi M, Mazzone M, Rezaei N. Pro-tumorigenic functions of macrophages at the primary, invasive and metastatic tumor site. Cancer Immunol Immunother 2020;69:1673–97.
18. Giraldo NA, Sanchez-Salas R, Peske JD, Vano Y, Becht E, Petitprez F, et al. The clinical role of the TME in solid cancer. Br J Cancer 2019;120:45–53.
19. Cendrowicz E, Sas Z, Bremer E, Rygiel TP. The role of macrophages in cancer development and therapy. Cancers (Basel) 2021;13:1946.
20. Casanova-Acebes M, Dalla E, Leader AM, LeBerichel J, Nikolic J, Morales BM, et al. Tissue-resident macrophages provide a pro-tumorigenic niche to early NSCLC cells. Nature 2021;595:578–84.
21. van Dalen FJ, van Stevendaal MHME, Fennemann FL, Verdoes M, Ilina O. Molecular repolarisation of tumour-associated macrophages. Molecules 2018;24:9.
22. Fujimura T, Kambayashi Y, Fujisawa Y, Hidaka T, Aiba S. Tumor-associated macrophages: therapeutic targets for skin cancer. Front Oncol 2018;8:3.
23. Cassetta L, Pollard JW. Targeting macrophages: therapeutic approaches in cancer. Nat Rev Drug Discov 2018;17:887–904.
24. Kloosterman DJ, Akkari L. Macrophages at the interface of the co-evolving cancer ecosystem. Cell 2023;186:1627–51.
25. Falleni M, Savi F, Tosi D, Agape E, Cerri A, Moneghini L, et al. M1 and M2 macrophages' clinicopathological significance in cutaneous melanoma. Melanoma Res 2017;27:200–10.
26. Zhao X, Qu J, Sun Y, Wang J, Liu X, Wang F, et al. Prognostic significance of tumor-associated macrophages in breast cancer: a meta-analysis of the literature. Oncotarget 2017;8:30576–86.
27. Yu M, Guan R, Hong W, Zhou Y, Lin Y, Jin H, et al. Prognostic value of tumor-associated macrophages in pancreatic cancer: a meta-analysis. Cancer Manag Res 2019;11:4041–58.
28. Leblond MM, Zdimerova H, Desponds E, Verdeil G. Tumor-associated macrophages in bladder cancer: biological role, impact on therapeutic response and perspectives for immunotherapy. Cancers (Basel) 2021;13:4712.
29. Liu M, Ren Y, Zhou Z, Yang J, Shi X, Cai Y, et al. The crosstalk between macrophages and cancer cells potentiates pancreatic cancer cachexia. Cancer Cell 2024;42:885–903.e4.
30. Chen X, Chen J, Zhang W, Sun R, Liu T, Zheng Y, et al. Prognostic value of diametrically polarized tumor-associated macrophages in multiple myeloma. Oncotarget 2017;8:112685–96.
31. Shen H, Liu J, Chen S, Ma X, Ying Y, Li J, et al. Prognostic value of tumor-associated macrophages in clear cell renal cell carcinoma: a systematic review and meta-analysis. Front Oncol 2021;11:657318.
32. Yang S, He P, Wang J, Schetter A, Tang W, Funamizu N, et al. A novel MIF signaling pathway drives the malignant character of pancreatic cancer by targeting NR3C2. Cancer Res 2016;76:3838–50.
33. O'Reilly C, Doroudian M, Mawhinney L, Donnelly SC. Targeting MIF in cancer: therapeutic strategies, current developments, and future opportunities. Med Res Rev 2016;36:440–60.
34. Penticuff JC, Woolbright BL, Sielecki TM, Weir SJ, Taylor JA III. MIF family proteins in genitourinary cancer: tumorigenic roles and therapeutic potential. Nat Rev Urol 2019;16:318–28.
35. Soumoy L, Kindt N, Ghanem G, Saussez S, Journe F. Role of macrophage migration inhibitory factor (MIF) in melanoma. Cancers (Basel) 2019;11:529.
36. Balogh KN, Templeton DJ, Cross JV. Macrophage Migration Inhibitory Factor protects cancer cells from immunogenic cell death and impairs anti-tumor immune responses. PLoS One 2018;13:e0197702.
37. Nobre CCG, de Araújo JMG, Fernandes TAAM, Cobucci RNO, Lanza DCF, Andrade VS, et al. Macrophage migration inhibitory factor (MIF): biological activities and relation with cancer. Pathol Oncol Res 2017;23:235–44.
38. Verjans E, Noetzel E, Bektas N, Schütz AK, Lue H, Lennartz B, et al. Dual role of macrophage migration inhibitory factor (MIF) in human breast cancer. BMC Cancer 2009;9:230.
39. Rooney MS, Shukla SA, Wu CJ, Getz G, Hacohen N. Molecular and genetic properties of tumors associated with local immune cytolytic activity. Cell 2015;160:48–61.
40. Patel SJ, Sanjana NE, Kishton RJ, Eidizadeh A, Vodnala SK, Cam M, et al. Identification of essential genes for cancer immunotherapy. Nature 2017;548:537–42.
41. Williams MJ, Werner B, Barnes CP, Graham TA, Sottoriva A. Identification of neutral tumor evolution across cancer types. Nat Genet 2016;48:238–44.
42. Kalaora S, Samuels Y. Cancer exome-based identification of tumor neo-antigens using mass spectrometry. Methods Mol Biol 2019;1884:203–14.
43. Jiang P, Gu S, Pan D, Fu J, Sahu A, Hu X, et al. Signatures of T cell dysfunction and exclusion predict cancer immunotherapy response. Nat Med 2018;24:1550–8.
44. Kalaora S, Lee JS, Barnea E, Levy R, Greenberg P, Alon M, et al. Immunoproteasome expression is associated with better prognosis and response to checkpoint therapies in melanoma. Nat Commun 2020;11:896.
45. Roumenina LT, Daugan MV, Noé R, Petitprez F, Vano YA, Sanchez-Salas R, et al. Tumor cells hijack macrophage-produced complement C1q to promote tumor growth. Cancer Immunol Res 2019;7:1091–105.
46. Tu J, Wang D, Zheng X, Liu B. Single-cell RNA datasets and bulk RNA datasets analysis demonstrated C1Q+ tumor-associated macrophage as a major and antitumor immune cell population in osteosarcoma. Front Immunol 2023;14:911368.
47. Xiong D, Wang Y, You M. A gene expression signature of TREM2^{hi} macrophages and γδ T cells predicts immunotherapy response. Nat Commun 2020;11:5084.
48. Zhang L, Li Z, Skrzypczynska KM, Fang Q, Zhang W, O'Brien SA, et al. Single-cell analyses inform mechanisms of myeloid-targeted therapies in colon cancer. Cell 2020;181:442–59.e29.
49. Revel M, Sautès-Fridman C, Fridman W-H, Roumenina LT. C1q+ macrophages: passengers or drivers of cancer progression. Trends Cancer 2022;8:517–26.
50. Fei F, Qu J, Zhang M, Li Y, Zhang S. S100A4 in cancer progression and metastasis: a systematic review. Oncotarget 2017;8:73219–39.

51. Zou Z, Hu X, Luo T, Ming Z, Chen X, Xia L, et al. Naturally-occurring spinosyn A and its derivatives function as argininosuccinate synthase activator and tumor inhibitor. Nat Commun 2021;12:2263.
52. Dubrot J, Du PP, Lane-Reticker SK, Kessler EA, Muscato AJ, Mehta A, et al. In vivo CRISPR screens reveal the landscape of immune evasion pathways across cancer. Nat Immunol 2022;23:1495–506.
53. Dubrot J, Lane-Reticker SK, Kessler EA, Ayer A, Mishra G, Wolfe CH, et al. In vivo screens using a selective CRISPR antigen removal lentiviral vector system reveal immune dependencies in renal cell carcinoma. Immunity 2021;54:571–85.e6.
54. Lane-Reticker SK, Kessler EA, Muscato AJ, Kim SY, Doench JG, Yates KB, et al. Protocol for in vivo CRISPR screening using selective CRISPR antigen removal lentiviral vectors. STAR Protoc 2023;4:102082.
55. Leng L, Metz CN, Fang Y, Xu J, Donnelly S, Baugh J, et al. MIF signal transduction initiated by binding to CD74. J Exp Med 2003;197:1467–76.
56. Figueiredo CR, Azevedo RA, Mousdell S, Resende-Lara PT, Ireland L, Santos A, et al. Blockade of MIF-CD74 signalling on macrophages and dendritic cells restores the antitumour immune response against metastatic melanoma. Front Immunol 2018;9:1132.
57. Wang K, Patkar S, Lee JS, Gertz EM, Robinson W, Schischlik F, et al. Deconvolving clinically relevant cellular immune cross-talk from bulk gene expression using CODEFACS and LIRICS stratifies patients with melanoma to anti-PD-1 therapy. Cancer Discov 2022;12:1088–105.
58. Saltz J, Gupta R, Hou L, Kurc T, Singh P, Nguyen V, et al. Spatial organization and molecular correlation of tumor-infiltrating lymphocytes using deep learning on pathology images. Cell Rep 2018;23:181–93.e7.
59. Sun D, Wang J, Han Y, Dong X, Ge J, Zheng R, et al. TISCH: a comprehensive web resource enabling interactive single-cell transcriptome visualization of tumor microenvironment. Nucleic Acids Res 2021;49:D1420–30.
60. Adams R, Osborn G, Mukhia B, Laddach R, Willsmore Z, Chenoweth A, et al. Influencing tumor-associated macrophages in malignant melanoma with monoclonal antibodies. Oncoimmunology 2022;11:2127284.
61. Porcellato I, Sforna M, Lo Giudice A, Bossi I, Musi A, Tognoloni A, et al. Tumor-associated macrophages in canine oral and cutaneous melanomas and melanocytomas: phenotypic and prognostic assessment. Front Vet Sci 2022;9:878949.
62. Kubota K, Moriyama M, Furukawa S, Rafiul H, Maruse Y, Jinno T, et al. CD163^{+}CD204^{+} tumor-associated macrophages contribute to T cell regulation via interleukin-10 and PD-L1 production in oral squamous cell carcinoma. Sci Rep 2017;7:1755.
63. Wang B, Liu H, Dong X, Wu S, Zeng H, Liu Z, et al. High CD204+ tumor-infiltrating macrophage density predicts a poor prognosis in patients with urothelial cell carcinoma of the bladder. Oncotarget 2015;6:20204–14.
64. Komohara Y, Hasita H, Ohnishi K, Fujiwara Y, Suzu S, Eto M, et al. Macrophage infiltration and its prognostic relevance in clear cell renal cell carcinoma. Cancer Sci 2011;102:1424–31.
65. Kaku Y, Imaoka H, Morimatsu Y, Komohara Y, Ohnishi K, Oda H, et al. Overexpression of CD163, CD204 and CD206 on alveolar macrophages in the lungs of patients with severe chronic obstructive pulmonary disease. PLoS One 2014;9:e87400.
66. Sugimoto M, Mitsunaga S, Yoshikawa K, Kato Y, Gotohda N, Takahashi S, et al. Prognostic impact of M2 macrophages at neural invasion in patients with invasive ductal carcinoma of the pancreas. Eur J Cancer 2014;50:1900–8.
67. A-Gonzalez N, Quintana JA, García-Silva S, Mazariegos M, González de la Aleja A, Nicolás-Ávila JA, et al. Phagocytosis imprints heterogeneity in tissue-resident macrophages. J Exp Med 2017;214:1281–96.
68. Mantovani A, Allavena P, Marchesi F, Garlanda C. Macrophages as tools and targets in cancer therapy. Nat Rev Drug Discov 2022;21:799–820.
69. Kindt N, Lechien JR, Nonclercq D, Laurent G, Saussez S. Involvement of CD74 in head and neck squamous cell carcinomas. J Cancer Res Clin Oncol 2014;140:937–47.
70. Lippitz BE. Cytokine patterns in patients with cancer: a systematic review. Lancet Oncol 2013;14:e218–28.
71. Conroy H, Mawhinney L, Donnelly SC. Inflammation and cancer: macrophage migration inhibitory factor (MIF)–the potential missing link. QJM 2010;103:831–6.
72. Rendon BE, Roger T, Teneng I, Zhao M, Al-Abed Y, Calandra T, et al. Regulation of human lung adenocarcinoma cell migration and invasion by macrophage migration inhibitory factor. J Biol Chem 2007;282:29910–8.
73. Meyer-Siegler KL, Iczkowski KA, Leng L, Bucala R, Vera PL. Inhibition of macrophage migration inhibitory factor or its receptor (CD74) attenuates growth and invasion of DU-145 prostate cancer cells. J Immunol 2006;177:8730–9.
74. Schrader J, Deuster O, Rinn B, Schulz M, Kautz A, Dodel R, et al. Restoration of contact inhibition in human glioblastoma cell lines after MIF knockdown. BMC Cancer 2009;9:464.
75. Piette C, Deprez M, Roger T, Noël A, Foidart J-M, Munaut C. The dexamethasone-induced inhibition of proliferation, migration, and invasion in glioma cell lines is antagonized by macrophage migration inhibitory factor (MIF) and can be enhanced by specific MIF inhibitors. J Biol Chem 2009;284:32483–92.
76. Ioannou K, Cheng KF, Crichlow GV, Birmpilis AI, Lolis EJ, Tsitsilonis OE, et al. ISO-66, a novel inhibitor of macrophage migration, shows efficacy in melanoma and colon cancer models. Int J Oncol 2014;45:1457–68.
77. Choudhary S, Hegde P, Pruitt JR, Sielecki TM, Choudhary D, Scarpato K, et al. Macrophage migratory inhibitory factor promotes bladder cancer progression via increasing proliferation and angiogenesis. Carcinogenesis 2013;34:2891–9.
78. Charan M, Das S, Mishra S, Chatterjee N, Varikuti S, Kaul K, et al. Macrophage migration inhibitory factor inhibition as a novel therapeutic approach against triple-negative breast cancer. Cell Death Dis 2020;11:774.
79. Liao Y, Wu C, Li Y, Wen J, Zhao D. MIF is a critical regulator of mononuclear phagocytic infiltration in hepatocellular carcinoma. iScience 2023;26:107273.
80. Hsu PD, Scott DA, Weinstein JA, Ran FA, Konermann S, Agarwala V, et al. DNA targeting specificity of RNA-guided Cas9 nucleases. Nat Biotechnol 2013;31:827–32.
81. Doench JG, Fusi N, Sullender M, Hegde M, Vaimberg EW, Donovan KF, et al. Optimized sgRNA design to maximize activity and minimize off-target effects of CRISPR-Cas9. Nat Biotechnol 2016;34:184–91.
82. Xu H, Xiao T, Chen C-H, Li W, Meyer CA, Wu Q, et al. Sequence determinants of improved CRISPR sgRNA design. Genome Res 2015;25:1147–57.
83. Concordet J-P, Haeussler M. CRISPOR: intuitive guide selection for CRISPR/Cas9 genome editing experiments and screens. Nucleic Acids Res 2018;46:W242–5.
84. Kalaora S, Barnea E, Merhavi-Shoham E, Qutob N, Teer JK, Shimony N, et al. Use of HLA peptidomics and whole exome sequencing to identify human immunogenic neo-antigens. Oncotarget 2016;7:5110–7.
85. Kalaora S, Wolf Y, Feferman T, Barnea E, Greenstein E, Reshef D, et al. Combined analysis of antigen presentation and T-cell recognition reveals restricted immune responses in melanoma. Cancer Discov 2018;8:1366–75.
86. Reynisson B, Alvarez B, Paul S, Peters B, Nielsen M. NetMHCpan-4.1 and NetMHCIIpan-4.0: improved predictions of MHC antigen presentation by concurrent motif deconvolution and integration of MS MHC eluted ligand data. Nucleic Acids Res 2020;48:W449–54.
87. Flynn RA, Belk JA, Qi Y, Yasumoto Y, Wei J, Alfajaro MM, et al. Discovery and functional interrogation of SARS-CoV-2 RNA-host protein interactions. Cell 2021;184:2394–411.e16.
88. Li H, Durbin R. Fast and accurate long-read alignment with Burrows-Wheeler transform. Bioinformatics 2010;26:589–95.

89. Li H, Handsaker B, Wysoker A, Fennell T, Ruan J, Homer N, et al. The sequence alignment/map format and SAMtools. Bioinformatics 2009;25:2078–9.
90. Jaitin DA, Kenigsberg E, Keren-Shaul H, Elefant N, Paul F, Zaretsky I, et al. Massively parallel single-cell RNA-seq for marker-free decomposition of tissues into cell types. Science 2014;343:776–9.
91. Kohen R, Barlev J, Hornung G, Stelzer G, Feldmesser E, Kogan K, et al. UTAP: user-friendly transcriptome analysis pipeline. BMC Bioinformatics 2019;20:154.
92. Robinson MD, Smyth GK. Moderated statistical tests for assessing differences in tag abundance. Bioinformatics 2007;23:2881–7.
93. McLaren W, Gil L, Hunt SE, Riat HS, Ritchie GRS, Thormann A, et al. The Ensembl variant effect predictor. Genome Biol 2016;17:122.
94. Law CW, Chen Y, Shi W, Smyth GK. voom: precision weights unlock linear model analysis tools for RNA-seq read counts. Genome Biol 2014;15:R29.
95. Subramanian A, Tamayo P, Mootha VK, Mukherjee S, Ebert BL, Gillette MA, et al. Gene set enrichment analysis: a knowledge-based approach for interpreting genome-wide expression profiles. Proc Natl Acad Sci U S A 2005;102:15545–50.
96. Jassal B, Matthews L, Viteri G, Gong C, Lorente P, Fabregat A, et al. The reactome pathway knowledgebase. Nucleic Acids Res 2020;48:D498–503.
97. Benjamini Y, Hochberg Y. Controlling the false discovery rate–a practical and powerful approach to multiple testing. J R Stat Soc B 1995;57:289–300.
98. Hänzelmann S, Castelo R, Guinney J. GSVA: gene set variation analysis for microarray and RNA-seq data. BMC Bioinformatics 2013;14:7.
99. Talevich E, Shain AH, Botton T, Bastian BC. CNVkit: genome-wide copy number detection and visualization from targeted DNA sequencing. PLoS Comput Biol 2016;12:e1004873.
100. Miller CA, White BS, Dees ND, Griffith M, Welch JS, Griffith OL, et al. SciClone: inferring clonal architecture and tracking the spatial and temporal patterns of tumor evolution. PLoS Comput Biol 2014;10:e1003665.
101. Shi W, Ng CKY, Lim RS, Jiang T, Kumar S, Li X, et al. Reliability of whole-exome sequencing for assessing intratumor genetic heterogeneity. Cell Rep 2018;25:1446–57.
102. Dang HX, White BS, Foltz SM, Miller CA, Luo J, Fields RC, et al. ClonEvol: clonal ordering and visualization in cancer sequencing. Ann Oncol 2017;28:3076–82.
103. Cancer Genome Atlas Network. Genomic classification of cutaneous melanoma. Cell 2015;161:1681–96.
104. Philip M, Fairchild L, Sun L, Horste EL, Camara S, Shakiba M, et al. Chromatin states define tumour-specific T cell dysfunction and reprogramming. Nature 2017;545:452–6.
105. Hao Y, Hao S, Andersen-Nissen E, Mauck WM III, Zheng S, Butler A, et al. Integrated analysis of multimodal single-cell data. Cell 2021;184:3573–87.e29.
106. Bunis DG, Andrews J, Fragiadakis GK, Burt TD, Sirota M. dittoSeq: universal user-friendly single-cell and bulk RNA sequencing visualization toolkit. Bioinformatics 2021;36:5535–6.
107. Azizi E, Carr AJ, Plitas G, Cornish AE, Konopacki C, Prabhakaran S, et al. Single-cell map of diverse immune phenotypes in the breast tumor microenvironment. Cell 2018;174:1293–308.e36.
108. Xu S, Hu E, Cai Y, Xie Z, Luo X, Zhan L, et al. Using clusterProfiler to characterize multiomics data. Nat Protoc 2024;19:3292–320.
109. Black S, Phillips D, Hickey JW, Kennedy-Darling J, Venkataraaman VG, Samusik N, et al. CODEX multiplexed tissue imaging with DNA-conjugated antibodies. Nat Protoc 2021;16:3802–35.
110. Bankhead P, Loughrey MB, Fernández JA, Dombrowski Y, McArt DG, Dunne PD, et al. QuPath: open source software for digital pathology image analysis. Sci Rep 2017;7:16878.
111. Schmidt U, Weigert M, Broaddus C, Myers G. Cell detection with star-convex polygons. In: Medical Image Computing and Computer Assisted Intervention – MICCAI. Cham: Springer; 2018. p. 265–73.
112. von Chamier L, Laine RF, Jukkala J, Spahn C, Krentzel D, Nehme E, et al. Democratising deep learning for microscopy with ZeroCostDL4Mic. Nat Commun 2021;12:2276.
113. Iyer A, Hamers AAJ, Pillai AB. CyTOF® for the masses. Front Immunol 2022;13:815828.
114. Li W, Xu H, Xiao T, Cong L, Love MI, Zhang F, et al. MAGeCK enables robust identification of essential genes from genome-scale CRISPR/Cas9 knockout screens. Genome Biol 2014;15:554.
115. Li B, Li JZ. A general framework for analyzing tumor subclonality using SNP array and DNA sequencing data. Genome Biol 2014;15:473.
116. Zhu Z, Li G, Li Z, Wu Y, Yang Y, Wang M, et al. Core immune cell infiltration signatures identify molecular subtypes and promote precise checkpoint immunotherapy in cutaneous melanoma. Front Immunol 2022;13:914612.
117. Therneau TM, Grambsch PM. Modeling Survival Data: Extending the Cox Model. New York (NY): Springer New York; 2000.